ENERGY TRANSFER AND DISSIPATION PROCESSES IN DOPED CRYSTALS

By

ROBERT GLEN PETERSON

Bachelor of Science
Brigham Young University
Provo, Utah
1971

Master of Science
Brigham Young University
Provo, Utah
1974

Submitted to the Faculty of the Graduate College
of the Oklahoma State University
in partial fulfillment of the requirements
for the Degree of
DOCTOR OF PHILOSOPHY
December, 1977

ENERGY TRANSFER AND DISSIPATION PROCESSES IN

DOPED CRYSTALS

Thesis Approved:

R. C. Powell
Thesis Adviser

Geoff P. Summ

James Lange

Kent Carney

Norman N. Durham
Dean of the Graduate College

ACKNOWLEDGMENTS

I would first like to thank my parents for the good influence they have had in my life. They have given me good, sound advice which I am happy to have followed. Their help and support, as well as that from the rest of my family, is deeply appreciated. I wish to thank my adviser, Dr. R. C. Powell, for his time and efforts. Although I have tried to write the chapters which discuss the energy transfer work in my own words, most of the understanding, interpretation of results, and sense of organization of these parts of the thesis came from two papers Dr. Powell has written. Much of the direction in determining the results of the photoacoustic work also came from him. Dr. G. F. Imbusch of University College in Ireland also helped in this regard. I wish to thank the members of my Advisory Committee, Dr. G. P. Summer, Dr. J. N. Lange, and Dr. K. L. Carraway for their help, and my colleague, Mr. M. Zokai, for helping to acquire some of the experimental results. I want to thank Mrs. Dolores Behrens for her help and expertise in typing the dissertation. My work was partially supported by a grant from the United States Army Research Office, for which I am grateful.

TABLE OF CONTENTS

LIST OF TABLES

LIST OF FIGURES

CHAPTER I

INTRODUCTION

Today's technology continues to advance at a rate which requires a continual need to understand the properties of materials and the development of new devices. This is true, of course, of optical materials and devices. The development of laser systems, for example, has progressed greatly since the laser's inception two decades ago. This is evidenced in the recent plans and designs of laser communication systems to transport information. Engineers and technologists developing new devices which incorporate optical materials will need to know beforehand what the basic properties of these materials are, and so continued research into the optical properties of materials is warranted.

Two of the basic processes which can be studied in many optical materials are host-sensitized energy transfer and nonradiative decay. These two processes will be the subjects of the present study.

The dissertation discusses two different investigations. The first part deals with host-sensitized energy transfer in rare-earth doped calcium tungstate crystals which have been laser excited in the long wavelength tail of the host absorption band. The method of Time-Resolved Spectroscopy (TRS) is used as the investigating tool.

The second part of the dissertation deals with investigating radiationless relaxation processes and avenues of decay in several

chromium-doped materials using the technique of Photoacoustic Spectroscopy (PAS).

The thesis is organized so that a discussion of the Förster-Dexter interaction theory of resonant energy transfer follows in Chapter II. Also in Chapter II appears one of the two prominent theories on the generation of the photoacoustic signal obtained in the study of solid materials. Chapter III contains a description of the samples and experimental apparatus. The results, summarized below, are discussed in more detail in Chapters IV and V. A brief summary is also given in Chapter VI.

Summary of Thesis

Time-Resolved Spectroscopy of $CaWO_4:Sm^{3+}$ and $CaWO_4:Eu^{3+}$

Tungstate molecular ions have been reported as the emission centers in $CaWO_4$, and the sources of its ultraviolet absorption band (1,2). Other results have indicated that tungstate ions next to activator impurities act as exciton traps, and that the type of host-sensitized energy transfer process taking place depends on the wavelength of excitation employed (3,4). These previous results were obtained for broadband excitation into the major host absorption bands, and indicated that at low temperatures energy was transferred from randomly distributed self-trapped excitons to randomly distributed activators in a single step process (3). The energy transfer taking place at high temperatures was determined to be a multistep exciton diffusion process with the activators acting as exciton traps. These results

also predicted the existence of extended trapping regions around each activator.

In the present study, calcium tungstate crystals doped with either trivalent samarium or europium impurities were excited in the long wavelength tail of the low energy host absorption band by a pulsed nitrogen laser emitting at 3371 Å. As is the case in Time-Resolved Spectroscopy, the ratios of the activator to host integrated fluorescence intensities were monitored versus time after the laser pulse. The model used to interpret the results is based on direct excitation of activator-induced tungstate defect sites. Energy is transferred from these sites to activators which are their nearest neighbors in a one step process. The energy transfer rates obtained from fitting the experimental results to this model are found to be equivalent to those determined by lifetime quenching measurements. The type of transfer mechanism involved could be either electric dipole-dipole or exchange interaction since each is capable of predicting sufficient energy transfer to account for the rates determined experimentally.

The idea that the type of host-sensitized energy transfer taking place is dependent upon the wavelength of excitation used is upheld by the fact that in the present case activator-induced tungstate defect sites are directly excited by the laser emission at 3371 Å and that the energy transfer then taking place is by a single step, nearest neighbor process, because these results differ from those obtained for higher energy excitation (3). The prediction of extended trapping regions around each activator (3) is also supported by the evidence of directly excitable activator-induced tungstate defect sites.

Photoacoustic Spectroscopy of $Al_2O_3:Cr^{3+}$, $MgO:Cr^{3+}$, $SrTiO_3:Cr^{3+}$ and $BaTiO_3:Cr^{3+}$

Energy which is absorbed by a solid and converted to heat by radiationless deexcitation processes will give rise to a signal in a photoacoustic spectrometer, if such energy is modulated in time. In a sealed cell, such a periodic heat flow will diffuse through the sample causing pressure fluctuations in the surrounding gas which can be detected by a microphone. If all of the absorbed energy is converted to heat, the subsequent spectrum will be comparable to an optical absorption spectrum. If, on the other hand, only a fraction of the absorbed energy exits radiationlessly, the resulting spectrum should be considered together with optical absorption and fluorescence excitation spectra to elucidate radiationless decay processes and modes of decay not evident in optical measurements.

A broadband tungsten-halogen source was used to periodically excite several host materials containing Cr^{3+} impurities. The PAS signal intensity as a function of wavelength was monitored as well as the relative phase of the signal, and these results are compared to the absorption and excitation spectra of the samples.

At least one earlier attempt has been made to extract PAS information from a ruby sample (5). Owing to this, ruby was used as the model system in the present study. Results indicate that there is radiationless decay from both the $^4T_1$ and $^4T_2$ chromium ion levels, with $S_{PAS}(^4T_1) > S_{PAS}(^4T_2)$, and that the $^4T_1$ level is resolved into its A and E components due to crystal field splitting. These results are consistent with those obtained earlier by other workers (5). A strong

band also appears in the region of the ^2E level. The origins of this band are not completely understood at this time. Analysis of the phase angles observed indicate a very fast mode of radiationless decay in ruby. There are two routes to radiationless decay present in this material, the first being a direct process from the excited energy levels to the ground state, and the second being a cascade through the levels until ^2E is reached which deexcites radiatively. Comparison of the rates observed in the PAS results with those calculated by others (6) indicates that the second mode of decay is preferred. This conclusion is substantiated by other reports (7) and calculated predictions performed herein.

A large radiationless contribution is also detected in the region of the ^2E level of $MgO:Cr^{3+}$. As in ruby, the origins of this signal require further study. The transitions monitored photoacoustically in $MgO:Cr^{3+}$ also exhibit fast lifetimes, however, calculations predict that the preferred route of decay here is not a simple cascade process, but is more complicated. The presence of a significant number of chromium ions occupying sites of orthorhombic site symmetry (8) is postulated as contributing to the problem.

The spectra of $SrTiO_3:Cr^{3+}$ and $BaTiO_3:Cr^{3+}$ are less conclusive since the Cr^{3+} absorption bands are probably hidden by other absorption in these crystals (9). No Cr^{3+} luminescence is detected in $BaTiO_3:Cr^{3+}$ and the PAS results are observed to mirror the optical absorption data.

Calculations using the PAS results indicate a trend towards increasing $^4T_2$ level contributions to radiationless decay as the static coupling to the lattice and the effects of crystal field splitting

decrease. The results are obtained by monitoring the change in certain parameters as the sample is changed from ruby to $SrTiO_3:Cr^{3+}$ to $MgO:Cr^{3+}$. A similar increasing trend in $^4T_2$ level participation in radiationless decay has been reported for successive increases in Cr^{3+} concentrations in $Al_2O_3:Cr^{3+}$ (5).

CHAPTER II

THEORETICAL

Energy Transfer by Exchange Interaction

Background

Energy transfer in solids refers to that process by which exciting radiation is absorbed by one type of ion, called the sensitizer S, and is transferred by some mechanism to another type of ion called the activator A. If S is a constituent of the host lattice, then the term "host-sensitized" transfer is applied. If S is an impurity, the process is called impurity-sensitized energy transfer.

The process of energy transfer can be divided into five steps (10): [1] absorption of a photon of energy E_o by the sensitizer, [2] relaxation of the lattice surrounding the sensitizer by an amount such that the available electronic energy in a radiative transition from the sensitizer is $E_1 < E_o$, [3] transfer of energy E_1 to the activator, [4a] relaxation around the activator such that the available electronic energy in a radiative transition is $E_2 < E_1$, [4b] relaxation around the sensitizer to a state similar (but not necessarily identical) to its original unexcited state, [5] emission of energy E_2.

There are four ways by which energy is transferred to the activator (step number three above) (11): [1] Photoconductivity - an ion

absorbs a photon of the exciting radiation creating a free electron and hole, either of which may travel through the lattice. [2] Radiative reabsorption - a photon of excitation is absorbed by an ion which later emits another photon. This second photon travels through the lattice until it is absorbed by another ion. [3] Long range resonant interaction - an ion which has been excited by absorbing a photon, interacts via a multipole-multipole or exchange interaction with another ion and subsequently transfers this quantum of excitation. [4] Exciton migration - at the absorbing ion a coupled electron-hole pair (exciton) is created which then migrates through the lattice carrying energy but not charge. At some other point in the lattice the pair recombine releasing the excitation energy.

Förster-Dexter Interaction Theory

Early work on energy transfer theory was performed by T. Förster (12,13). Later, D. L. Dexter examined the mechanism of energy transfer on the basis of a long range resonance theory which will be followed closely below (10).

According to time-dependent perturbation theory the transition probability per unit time can be expresses as

$$P_{SA} = (2\pi/\hbar)\left|\langle H_1 \rangle\right|^2 \rho_E$$

where $\langle H_1 \rangle$ is the matrix element of the perturbation to the Hamiltonian, between the initial and final states of the system, and ρ_E is the density of states. The initial state of the system, Ψ_I, is such that the sensitizer S is excited, ψ_S^*, while the activator A is in its ground

state, ψ_a. The final state, Ψ_F, is assigned the configuration in which S is in its ground state, ψ_s, while A is excited, ψ_a'. (The primed quantities refer to excited states.) The transition probability of transfer from a particular S to a particular A is written,

$$P_{SA} = (2\pi/\hbar)\rho_E \left| \int \Psi_I^* \, H_1 \, \Psi_F d\tau \right|^2 \qquad (1)$$

under the assumption that states Ψ_I and Ψ_F are of the same energy.

Due to lattice vibrations, the energy levels of S and A are not well defined, behaving more as continuous bands than discrete levels. Under these conditions, the wave functions are normalized on an energy scale and the density of states factor is included within the normalization parameters. The properly antisymmetrized initial and final states wave functions describing S and A can be written, assuming only two electrons are involved, as

$$\begin{aligned} \Psi_I(\omega_s', \omega_a) &= (1/\sqrt{2})[\psi_s'(\bar{r}_1, \omega_s')\psi_a(\bar{r}_2, \omega_a) \\ &\quad - \psi_s'(\bar{r}_2, \omega_s')\psi_a(\bar{r}_1, \omega_a)] \\ \Psi_F(\omega_s, \omega_a') &= (1/\sqrt{2})[\psi_s(\bar{r}_1, \omega_s)\psi_a'(\bar{r}_2, \omega_a') \\ &\quad - \psi_s(\bar{r}_2, \omega_s)\psi_a'(\bar{r}_1, \omega_a')] \end{aligned} \qquad (2)$$

The $\bar{r}_i$ represent the coordinates of the electrons involved, and the ω_j represent the energy of the wave functions.

Conservation of energy is assumed, such that $E=\omega_s'-\omega_s=\omega_a'-\omega_a$. Thus the probability P_{SA} must contain a Dirac delta-function $\delta[(\omega_s'-\omega_s) - (\omega_a'-\omega_a)]$. With this inclusion, and expressing the matrix element of

H_1 between states $\Psi_I(\omega_s', \omega_a)$ and $\Psi_F(\omega_s, \omega_a')$ as $\langle H_1(\omega_s', \omega_a; \omega_s, \omega_a')\rangle_{IF}$, the probability of energy transfer from S to A is given by

$$P_{SA} = (2\pi/\hbar) \sum_I \sum_F (g_s' g_a)^{-1} \bullet \int d\omega_a' \int d\omega_s \int d\omega_a p_a(\omega_a) \int d\omega_s' p_s'(\omega_s') \bullet \left| \langle H_1(\omega_s', \omega_a; \omega_s, \omega_a')\rangle_{IF} \right|^2 \bullet \delta[(\omega_s' - \omega_s) - (\omega_a' - \omega_a)] \quad (3)$$

The factors g_s' and g_a represent the degree of degeneracy of the two levels respectively. The parameters $p_s'(\omega_s')$ and $p_a(\omega_a)$ express the probabilities that S is in the particular energy state ω_s' and that A is in the state ω_a. The sums over I and F represent a sum over all possible transitions that can contribute to energy transfer. Carrying out the integration, making use of the delta function, yields

$$P_{SA} = (2\pi/\hbar) \sum_I \sum_F (g_s' g_a)^{-1} \bullet \int dE \int d\omega_a p(\omega_a) \int d\omega_s' p_s'(\omega_s') \bullet \left| \langle H_1(\omega_s', \omega_a; \omega_s' - E, \omega_a + E)\rangle_{IF} \right|^2 \quad (4)$$

Dipole-Dipole Interaction

The wave functions of Equation (2) contain both Coulomb terms and terms which enter because of antisymmetrization, the exchange terms. It is common practice (10) to calculate first the transfer probability due to the Coulomb terms leading to electric multipole interactions.

This requires a knowledge of H_1, the interaction between A and S. H_1 is defined as the sum of all the Coulomb interactions of the outer electrons and core of the activator with those of the sensitizer. The sum is expanded in a Taylor series about the nuclear separation distance, $\bar{R}$, between activator and sensitizer. Consideration has also been made for any reduction of the interaction by the dielectric constant of the medium by introducing the dielectric constant k. The interaction becomes

$$\begin{aligned} H_1(\bar{R}) = {} & (e^2/kR^3)\left\{\bar{r}_s\cdot\bar{r}_a - 3(\bar{r}_s\cdot\bar{R})(\bar{r}_a\cdot\bar{R})/R^2\right\} \\ & + (3e^2/2kR^4)\left\{\sum_{i=1}^{3}(R_i/R)r_{ai}^2 r_{si}(-3+5R_i^2/R^2)\right. \\ & + 10(XYZ/R^3)(x_a y_a z_s + x_a z_a y_s + y_a z_a x_s) \\ & \left. + \sum_{i\neq j}^{3}\sum^{3}[(R_j/R)-5R_i^2R_j/R^3][-r_{ai}^2 r_{sj} - 2r_{ai}r_{aj}r_{si}]\right\} \\ & + ... \end{aligned} \tag{5}$$

This is the familiar multipole expansion, where the first term in curly brackets is the dipole-dipole term and the second set of curly brackets delineates the dipole-quadrupole interaction. Higher order interaction terms have been omitted.

Under the assumption of an allowed transition the dipole-dipole term gives the largest contribution. Inserting the first term of Equation (5) into Equation (4) yields

$$P_{SA}(dd) = (2\pi/\hbar)\sum_{I}\sum_{F}(e^4/k^2R^6)(g_s' g_a)^{-1}$$

$$\bullet \int dE \int d\omega_a p_a(\omega_a) \int d\omega_s' p_s'(\omega_s')$$

$$\bullet \left| \langle \bar{r}_s \rangle \cdot \langle \bar{r}_a \rangle - 3(\langle \bar{r}_s \rangle \cdot \bar{R})(\langle \bar{r}_a \rangle \cdot \bar{R})/R^2 \right|^2 \qquad (6)$$

The next step is to average the absolute square of the matrix element in Equation (6) over all possible orientations of $\bar{R}$

$$\left\langle \left| \langle \bar{r}_s \rangle \cdot \langle \bar{r}_a \rangle - (3/R^2)(\langle \bar{r}_s \rangle \cdot \bar{R})(\langle \bar{r}_a \rangle \cdot \bar{R}) \right|^2 \right\rangle_{avg}$$

$$= (2/3) \left| \langle \bar{r}_s \rangle \right|^2 \left| \langle \bar{r}_a \rangle \right|^2 \qquad (7)$$

The transfer probability then becomes

$$P_{SA}(dd) = \frac{4\pi e^4}{3\hbar k^2 R^6 g_s' g_a} \sum_I \sum_F \int dE$$

$$\bullet \left\{ \int d\omega_s' p_s(\omega_s') \left| \langle \bar{r}_s \rangle \right|^2 \right\}$$

$$\bullet \left\{ \int d\omega_a p_a(\omega_a) \left| \langle \bar{r}_a \rangle \right|^2 \right\} \qquad (8)$$

The matrix elements of Equation (8) are related to experimentally measurable quantities, such as absorption coefficients and decay times, in the following manner:

The probability of a spontaneous radiative transition of an isolated atom from a state i to a state f is given by Einstein's A coefficient

$$A(if) = \frac{4e^2 E^3}{3\hbar^4 C^3} \left| \langle \bar{r}_{if} \rangle \right|^2 \qquad (9)$$

For an atom in a crystal this expression is subject to some refinement (10) and becomes

$$A(E) = \sum_i \sum_f \frac{4e^2 E^3}{3\hbar^4 C^3 g'} \left(\frac{\varepsilon_c}{\varepsilon} \right)^2 n^3 \int \left| \langle \bar{r}_{if} \rangle \right|^2 p'(\omega') d\omega' \qquad (10)$$

where $(\varepsilon_c/\varepsilon)$ is the ratio of the electric field within the crystal to that of an isolated atom. n is the index of refraction of the medium and g′ is a degeneracy factor as has been previously introduced. The integral $\int A(E)dE$ is equal to the decay constant of the level, $1/\tau$, the inverse of the fluorescence lifetime. A normalized function f(E), representing the observed shape of the emission band can be introduced such that $\int f(E)dE=1$, a result which is related to the integrated fluorescence intensity of the sensitizer (11). Then from Equation (10)

$$\sum_i \sum_f \int \left| \langle \bar{r}_{if} \rangle \right|^2 p'(\omega')d\omega' = \frac{3\hbar^4 c^3 g'}{4n^2 e^2 E^3} \left(\frac{\varepsilon}{\varepsilon_c} \right)^2 \frac{1}{\tau} f(E) \qquad (11)$$

This equation is general in nature, referring to either the sensitizer or activator. However, the left-hand side of Equation (11) refers directly to S in Equation (8) and can be evaluated by measuring the decay time and emission spectrum of S under certain restrictive conditions (10).

For an isolated atom Einstein's B coefficient is

$$B(if) = \frac{2\pi e^2}{3\hbar^2} \left| \langle \bar{r}_{if} \rangle \right|^2 \qquad (12)$$

For a crystalline medium

$$B(E) = \sum_i \sum_f \frac{2\pi e^2}{3\hbar^2 g} \left(\frac{\varepsilon_c}{\varepsilon} \right)^2 \int p(\omega)d\omega \left| \langle \bar{r}_{if} \rangle \right|^2 \qquad (13)$$

The absorption cross section is $\sigma(E)=nhEB(E)/c$ so that

$$\sigma(E) = \sum_i \sum_f \frac{4\pi^2 e^2 nE}{3hcg} \left(\frac{\varepsilon_c}{\varepsilon} \right)^2 \int p(\omega)d\omega \left| \langle \bar{r}_{if} \rangle \right|^2 \qquad (14)$$

As in the previous case, a normalized function F(E) is introduced such that $\sigma(E)=QF(E)$ and $\int F(E)dE=1$. Thus

$$\sum_i \sum_f \int p(\omega)d\omega \left|\langle r_{if}\rangle\right|^2 = \frac{3\hbar cg}{4\pi^2 e^2 nE}\left(\frac{\varepsilon}{\varepsilon_c}\right)^2 QF(E) \qquad (15)$$

Equation (15) can be applied to the activator, assuming it has an observable absorption band, and the remaining matrix elements of Equation (8) can then be evaluated. $Q=\int\sigma(E)dE$ is defined as the integrated area under the absorption band.

Substitution of Equations (11) and (15) into Equation (8) yields

$$P_{SA}(dd) = \frac{3\hbar^4 c^4 Q_a}{4\pi R^6 n^4 \tau_s k^2}\left(\frac{\varepsilon}{\varepsilon_c}\right)^4 \int \frac{f_s(E)F_a(E)}{E^4}\,dE \qquad (16)$$

where use is made of absorption data for A and emission data for S. Equation (16) can be simplified (12,13) to

$$P_{SA}(dd) = \frac{1}{\tau_s^o}\left(\frac{R_o}{R}\right)^6 \qquad (17)$$

where (3,4)

$$R_o = \left[(5.86\times10^{-25}\ \phi_s/n^4)\int \frac{f_s(E)F_a(E)}{E^4}\,dE\right]^{1/6}.$$

R_o is called the critical transfer distance and is defined as the distance at which energy transfer between an isolated sensitizer-activator pair occurs at the same rate as the spontaneous decay of the sensitizer in the absence of activators, ϕ_s is the quantum efficiency of the sensitizer, the integral expresses the spectral overlap, and the numerical factor appears for dimensional consistency and contains

an orientation factor for averaging over a random distribution of dipoles.

Exchange Interaction

When considering exchange interactions the effects of electron spin enter in requiring the matrix element of the interaction Hamiltonian be written out in terms of wave functions of the type $\psi(\bar{r},\bar{\sigma}) = \phi(\bar{r})X(\bar{\sigma})$, where $X(\bar{\sigma})$ are the spin wave functions; (see Equation (2))

$$\begin{aligned}\langle H_1 \rangle = &\int \phi_s'^*(\bar{r}_1)\phi_a^*(\bar{r}_2)H_1\phi_s(\bar{r}_1)\phi_a'(\bar{r}_2) \\ &\bullet\ X_s'^*(\bar{\sigma}_1)X_a^*(\bar{\sigma}_2)X_s(\bar{\sigma}_1)X_a'(\bar{\sigma}_2) \\ &-\int \phi_s'^*(\bar{r}_1)\phi_a^*(\bar{r}_2)H_1\phi_a'(\bar{r}_1)\phi_s(\bar{r}_2) \\ &\bullet\ X_s'^*(\bar{\sigma}_1)X_a^*(\bar{\sigma}_2)X_a'(\bar{\sigma}_1)X_s(\bar{\sigma}_2) \qquad (18)\end{aligned}$$

The first integral in Equation (18) is the Coulomb term which was discussed in the previous section. The second term is an exchange integral with $H_1=e^2/kr_{12}$ and represents the electrostatic interaction between the two charge clouds

$$Q'(\bar{r}_1) = \phi_s'^*(\bar{r}_1)\phi_a'(\bar{r}_1) \text{ and } Q(\bar{r}_2) = \phi_a^*(\bar{r}_2)\phi_s(\bar{r}_2) \ ,$$

ignoring the spin parts. The spin wave functions serve to determine the selection rules in the exchange integrals. Previously, unless $X_s'=X_s$ and $X_a=X_a'$, the Coulomb integral vanished. In the case of exchange, unless $X_s'=X_a'$ and $X_a=X_s$, the second or exchange integral vanishes. However, X' need not be equal to X in exchange, so that

the spin functions on both atoms may change simultaneously. Therefore, even though the Coulomb terms vanish, indicating a forbidden multiple transition, exchange will allow transfer to and excitation of an activator by any allowed or forbidden transition.

The transfer probability by exchange interaction can be calculated using the methods of the previous section and is expressed as

$$P_{SA}(ex) = (2\pi/\hbar)Z^2 \int f_s(E)F_a(E)dE \tag{19}$$

where

$$Z^2 = \sum_I \sum_F \frac{1}{g_s' g_a k^2} \left| \int Q'(\bar{r}_1) \frac{e^2}{r_{12}} Q(\bar{r}_2) d\tau_{12} \right|^2_{IF} \tag{20}$$

Z^2 cannot be measured experimentally. However, Dexter (10) determines that $Z^2 \sim (e^4/k^2R_o^2)$ exp (-2R/L) where L is an effective average hydrogen-like Bohr radius and R is the conventional nuclear separation between S and A. Inokuti and Hirayama (14) express this quantity as $Z^2 = K^2$ exp (-2R/L) and derive an expression for the transfer probability by exchange which is written

$$P_{SA}(ex) = (1/\tau_o) \exp \left\{ \gamma[1-(R/R_o)] \right\} \tag{21}$$

where

$$\gamma = 2R_o/L$$

and

$$\frac{e^\gamma}{\tau_o} = \frac{2\pi}{\hbar} K^2 \int f_s(E)F_a(E)dE \tag{22}$$

The quantities R and L are as previously explained, and R_o is the so-called critical transfer distance for exchange interaction.

Photoacoustic Spectroscopy of Solids

Background

Photoacoustic spectroscopy of solids reemerged as a spectroscopic tool in 1973 (15). It is especially useful for those cases in medicine, biology, chemistry, and physics where sample preparation is a problem (16,17,18,19). In these cases PAS has generally been used to produce absorption spectra. Lately several workers have extended the uses of PAS to the elucidation of radiationless relaxation processes in solids (5,20).

The photoacoustic signal is generated in the following manner: Periodically modulated light is focused onto the sample which is contained within an enclosed cell filled with a transparent gas. The fraction of the absorbed light which contributes to radiationless deexcitation processes (the heating mode) will cause the sample to be periodically heated. The periodic heat flow in the sample will diffuse to the surrounding gas. This cyclical heating of the gas causes pressure fluctuations in the gas which are detected by a sensitive microphone mounted in the cell wall.

There are two main theoretical treatments of PAS in solids. The first is that of J. G. Parker (15) later amended by Parker and colleagues (21). The other is the theory advanced by Rosencwaig and Gersho (22). Either treatment gives comparable results and the choice of which to follow depends generally on the whims of the reader.

Theory

Following the theoretical treatment by Parker (15,21) Figure 1 shows the pertinent cell geometry. Periodically chopped light is absorbed by the solid (region three) which produces heat in the sample. This heat diffuses through the solid and into the gas (region two) and backing (region four). Thermal diffusion in the window (region one) is also considered.

The temperature in regions one and four is governed by the thermal transport equation

$$\alpha_i \nabla^2 T_i - \frac{\partial T_i}{\partial t} = 0 \qquad (23)$$

α_i (cm^2/sec) represents the thermal diffusivity in region i and is defined as (22) $\alpha_i = \kappa/\rho_i C_i$, where κ_i is the thermal conductivity, ρ_i is the density of the material, and C_i, the specific heat. For a one-dimensional case Equation (23) has solutions of the form $T_i = \exp(k_i x)$ where $k_i = (j\omega/\alpha_i)^{1/2}$ assuming T_i varies sinusoidally with time at chopping frequency ω. Therefore, solutions in regions one and four are

$$\begin{aligned} T_1 &= T_{10} \exp[k_w(L+x)] \qquad (x \leq -L; k_w = k_1) \\ T_4 &= T_{40} \exp[k_b(\ell_s - x)] \qquad (x \geq \ell_s; k_b = k_4) \end{aligned} \qquad (24)$$

In region two, assuming negligible gas viscosity,

$$\kappa_2 \nabla^2 T_2 - j\omega C_{p2} T_2 = -j\omega p_e \qquad (25)$$

κ_2 is the gas thermal conductivity, C_{p2} is the specific heat at constant pressure per unit volume, and p_e is the differential pressure.

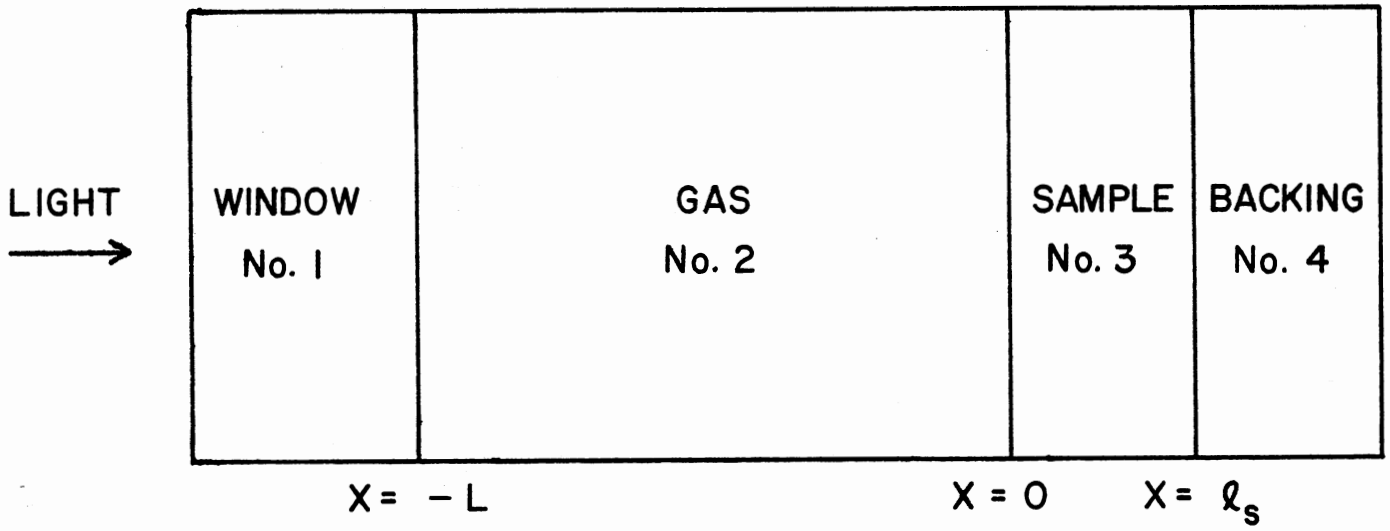

Figure 1. Cross Sectional Representation of a Theoretical Photoacoustic Cell Showing Pertinent Regions Described in the Theoretical Treatment

Through use of the equations of state and continuity the gas thermal transport equation may be written

$$j(\kappa_g/\omega)\nabla^4 T_g+[C_{pg}+j(\gamma\kappa_g/\omega)k_o^2]\nabla^2 T_g+k_o^2 C_{pg}T_g = 0 \qquad (26)$$

where γ is the ratio of specific heats, κ_g is the thermal conductivity, C_{pg} is the heat capacity of the gas, and $k_o=\omega/c_o$, c_o being the velocity of sound given by $c_o=(\gamma p_o/\rho_o)^{\frac{1}{2}}$. In the latter expression p_o is the ambient pressure and ρ_o the corresponding density.

The solution of Equation (26) may be written as

$$T_2 = T_{20} + T_{21} \qquad (27)$$

where T_{20} is the acoustic component satisfying

$$\nabla^2 T_{20} + k_o^2 T_{20} = 0 \qquad (28)$$

and T_{21} is the thermal wave satisfying

$$\nabla^2 T_{21} + k_g^2 T_{21} = 0 \qquad (29)$$

with $k_g = (j\omega C_{pg}/\kappa_g)^{\frac{1}{2}}$.

The differential pressure is

$$p_e(x) = d_o T_{20} + d_1 T_{21} \qquad (30)$$

where $d_o \approx C_{pg}$ and $d_1 = -j(\gamma-1)(\omega\kappa_g/c_o^2)$.

The solutions of Equations (28) and (29) can be written

$$T_{20} = A_2 \exp(-jk_o x) + B_2 \exp(jk_o x) \qquad (31)$$

and

$$T_{21} = C_2 \exp(-k_g x) \tag{32}$$

for a one-dimensional case, and the gas temperature becomes

$$T_g = E \cos k_o x + F \sin k_o x + G \cosh k_g x + H \sinh k_g x \tag{33}$$

where E, F, G and H are constants determined by the boundary conditions.

The thermal transport equation for the solid is

$$\alpha_s \nabla^2 T_s - \frac{\partial T_s}{\partial t} = \frac{H_s(x)}{C_{ps}} \tag{34}$$

where C_{ps} is the sample thermal capacity (watt-sec/cm^3) and H_s is the rate of heat input (watts/cm^3).

Light is absorbed in the sample according to the relation $I=I_o \exp(-\beta x)$, where I_o is the incident intensity, β the optical absorption coefficient, and x the thickness of the sample. The rate of energy loss per unit penetration is

$$\frac{dI}{dx} = -\beta I \tag{35}$$

and $H_s=\alpha(x)\beta I$, where $\alpha(x)$ is the fraction of light energy converted to heat.

If I is harmonic in time T will be also and Equation (34) can be written, in one dimension, as

$$\alpha_s \frac{\partial^2 T_s}{\partial x^2} - j\omega T_s = \frac{\alpha\beta I_o}{C_{ps}} \exp(-\beta x) \tag{36}$$

The exponential dependence of I can be eliminated by substituting the relation $T_s=u \exp(-\beta x)$ into Equation (36), resulting in

$$\alpha_s \left[\frac{\partial^2 u}{\partial x^2} - 2\beta \frac{\partial u}{\partial x} + \beta^2 u \right] - j\omega u = \frac{\alpha\beta I_o}{C_{ps}} \tag{37}$$

which has the particular solution $u=\alpha\beta I_o/(\beta^2-k_s^2)\kappa_s$ and the homogeneous solution $u=\exp(\beta+k_s)x$ where $k_s=(j\omega/\alpha_s)^{\frac{1}{2}}$. With these solutions the temperature of the solid can be written

$$T_s = M \cosh k_s x + N \sinh k_s x + T_o \tag{38}$$

given that

$$T_o = \alpha\beta I_o \exp(-\beta x)/(\beta^2-k_s^2)\kappa_s \tag{39}$$

The boundary conditions are those of temperature and heat flux continuity:

$$\kappa_i \frac{\partial T_i}{\partial x} = \kappa_j \frac{\partial T_j}{\partial x} \tag{40}$$

$$T_i = T_j \tag{41}$$

The indices i and j signify the two regions meeting at the interface. Applying the boundary conditions at x=-L and $x=\ell_s$ gives

$$\kappa_\omega k_\omega T_g(-L) = \kappa_g \frac{\partial T_g}{\partial x}(-L) \tag{42}$$

$$\kappa_b k_b T_s(\ell_s) = \kappa_s \frac{\partial T_s}{\partial x}(\ell_s) \tag{43}$$

Applying the same conditions at x=0 yields

$$T_s(o) = T_g(o) \tag{44}$$

$$\kappa_s \frac{\partial T_s(o)}{\partial x} = \kappa_g \frac{\partial T_g(o)}{\partial x} \tag{45}$$

Since the gas velocity, $v = \frac{j}{\omega\rho_o} \frac{\partial p_e}{\partial x}$ is zero at x=0 and x=-L

$$\left(\frac{\partial p_c}{\partial x}\right)_{x=-L} = \left(\frac{\partial p_e}{\partial x}\right)_{x=0} = 0 \tag{46}$$

This leads to the following two equations:

$$d_o \frac{\partial T_{20}(-L)}{\partial x} + d_1 \frac{\partial T_{21}(-L)}{\partial x} = 0 \tag{47}$$

$$d_o \frac{\partial T_{20}(o)}{\partial x} + d_1 \frac{\partial T_{21}(o)}{\partial x} = 0 \tag{48}$$

Substitution of Equations (33) and (38) into Equations (42), (43), (44), (45), (47) and (48) produces six simultaneous equations involving E, F, G, H, M, N, $T_o(o)$, $T_o(\ell_s)$, $\partial T_o(o)/\partial x$, and $\partial T_o(\ell_s)/\partial x$. If these equations are solved for E, F, G, and H and the solutions substituted into Equation (30) there results an expression for the photoacoustic signal of the form

$$S_{(PAS)} \propto p_e(-L) = Ag \tag{49}$$

where

$$A = \alpha\beta I_o[k_s - \beta\Gamma - Q(k_s - \beta\xi)\exp(-\beta\ell_s)]/k_s\kappa_s(\beta^2 - k_s^2) \tag{50}$$

is a factor which depends on such properties as optical absorption coefficient, sample length, sample thermal properties and, if an optically and thermally thin sample is used, on the thermal properties of the sample backing as well. The factor g is a sensitivity factor determined by cell parameters such as cell length and window and gas thermal properties, and is expressed as

$$g = \frac{[d_o-d_1][C_2-C_1+D(S_2+\eta S_1)]}{2(C_2C_1-1)+\varepsilon S_2S_1(1-\varepsilon^{-2}+BD\Gamma q^2)+q(D+B\Gamma)(\varepsilon S_1C_2+S_2C_1)} \qquad (51)$$

The symbols appearing in Equations (50) and (51) have the following meanings:

$C_1 = \cos k_o L$ $\qquad$ $S_1 = \sin k_o L$

$C_2 = \cosh k_g L$ $\qquad$ $S_2 = \sinh k_g L$

$C_4 = \cosh k_g \ell_s$ $\qquad$ $S_4 = \sinh k_s \ell_s$

$$B = \frac{\kappa_g k_g}{\kappa_s k_s} \qquad D = \frac{\kappa_g k_g}{\kappa_w k_w} \qquad \xi = \frac{\kappa_s k_s}{\kappa_b k_b}$$

$$\Gamma = \frac{\xi+(1-\xi^2)S_4C_4}{1+(1-\xi^2)S_4^2} \qquad Q = (C_4+\xi S_4)^{-1}$$

$$\eta = k_o/k_g = (\omega a_g/jc_o^2)^{\frac{1}{2}}$$

$$\varepsilon = d_o k_o/d_1 k_g = 1/(\gamma-1)\eta$$

$$q = 1-(\gamma-1)\eta^2$$

Equations (49), (50) and (51) show that the PAS signal can be written as

$$S_{PAS} = \alpha(\lambda)I_o(\lambda)\beta(\lambda)h\nu F(\beta,k_s\ell_s)G(k_g,\ell_g) \qquad (52)$$

where $I_o(\lambda)$ is the incident light intensity at wavelength λ, $\beta(\lambda)$ is the optical absorption coefficient, $\alpha(\lambda)$ is the fraction of absorbed light converted to heat (5), and $h\nu$ is the energy of the radiationless transition. F and G reflect the dependence upon certain physical parameters such as cell length, sample thickness and thermal diffusion lengths.

If the experiments are always carried out under equivalent conditions then F and G are no more than multiplicative constants and $S_{PAS} \propto \alpha\beta I_o(\lambda)h\nu$. This indicates that a simple normalization procedure results from dividing out the factor $I_o(\lambda)$ and the normalized PAS signal is proportional to the product $\alpha\beta h\nu$ (5).

Rosencwaig and Gersho (22) try to gain physical insight into their analogous expression to Equation (49) based on the relation of the optical absorption length $1/\beta$ to the thickenss of the solid. Their treatise is instructive but beyond the scope of this thesis.

Merkle and Powell (20) present an interesting method of predicting the lifetime of a particular excited state by determining the phase of the PAS signal. According to this theory the PAS signal at phase angle θ can be expressed as the sum of all the transitions decaying through the heating mode,

$$S_{PAS}(\theta) \propto N_a \sum_i \alpha_i \, h\nu_i \cos(\Omega_i - \theta)/N_o h\nu_o \qquad (53)$$

N_a is the number of photons absorbed, α_i is the fraction of excited atoms relaxing through the ith type of radiationless transition, $h\nu_i$ is the energy generated per phonon emitted, and Ω_i is the phase angle at which the signal due to transitions from the initial state of the ith transition is maximum. The factor $N_o h\nu_o$ is introduced for normalization purposes. The phase angle θ at which the signal is maximum is related to the lifetime of the state through the expression $\tau = \tan\theta/2\pi\nu_c$, where ν_c is the chopping frequency. (See (20) for earlier references to this latter result.)

CHAPTER III

SAMPLES AND APPARATUS

Although the TRS and PAS experiments of this thesis are quite dissimilar, they have some of the experimental equipment in common and will therefore be described together under a single heading.

The host-sensitized energy transfer results were obtained from work performed on three optical quality single crystal samples. These consisted of an undoped calcium tungstate sample and a $CaWO_4$ sample containing 0.5% Sm^{3+}, both obtained from Lambda/Airtron, and a $CaWO_4$ sample doped with 0.5% Eu^{3+} obtained from Raytheon. The rare earth impurity ions go into the lattice substitutionally for the host Ca^{2+} ions and are charge compensated by an equal concentration of Na^{+} ions. Sample thicknesses were 2.7mm, 2.6mm, and 3.1mm respectively.

Photoacoustic Spectroscopy was performed on four separate host materials each containing Cr^{3+} as the impurity. These are listed as follows: [1] An unpolished, 1.9mm thick piece of commercially available ruby laser rod doped with 0.01% Cr^{3+} ions. These go into the lattice substitutionally for the Al^{3+} ions. $Al_2O_3:Cr^{3+}$ possesses trigonal symmetry. [2] A polished single crystal sample of $SrTiO_3:Cr^{3+}$ (0.02% wt.) with a thickness of 1.3mm, obtained from National Lead Co. Strontium titanate possesses cubic symmetry at room temperature and tetragonal symmetry below 110K (9,12). The chromium ions replace Ti^{4+} with charge compensation occurring nonlocally (9,23). [3] An

unpolished single crystal and powdered samples of $MgO:Cr^{3+}$ (0.01%) obtained from Mussel Shoals. Thickness of the single crystal was 1.7mm. In this material Cr^{3+} substitutes for Mg^{2+} with positive ion vacancies for charge compensation (8,24). $MgO:Cr^{3+}$ possesses cubic symmetry to a first approximation. [4] Unpolished single crystal specimens of $BaTiO_3:Cr^{3+}$, with nominal thickness of 0.8mm, and powdered samples of the same. Cr^{3+} concentration was on the order of 0.02% wt. The samples were obtained from Lambda/Airtron. $BaTiO_3:Cr^{3+}$ possesses tetragonal symmetry at room temperature.

The powdered samples named above were used in the photoacoustic spectrometer only, to enhance the signal strength. All other measurements were performed on the single crystal samples.

When required, sample temperature control was maintained by an Air Products and Chemicals Displex CS202 Cryogenic Refrigerator system. The temperature was detected using a Chromel vs. gold - 0.07 at. % iron thermocouple.

All optical absorption measurements were made on a Cary 14 Spectrophotometer which uses a 1P28 photodetector in the ultraviolet (2000-3500 Å) and visible (3500-6500 Å) regions, and a PbS cell in the infrared (>6500 Å). U.V. radiation is provided by a deuterium lamp and a tungsten-halogen lamp provides the visible and I.R. illumination.

Figure 2 shows the block diagram of the experimental set-up of the laser Time-Resolved Spectroscopy system used in the energy transfer work. The 3371 Å emission of a pulsed nitrogen laser was focused on the sample which was mounted to the cold-end of the cryogenic

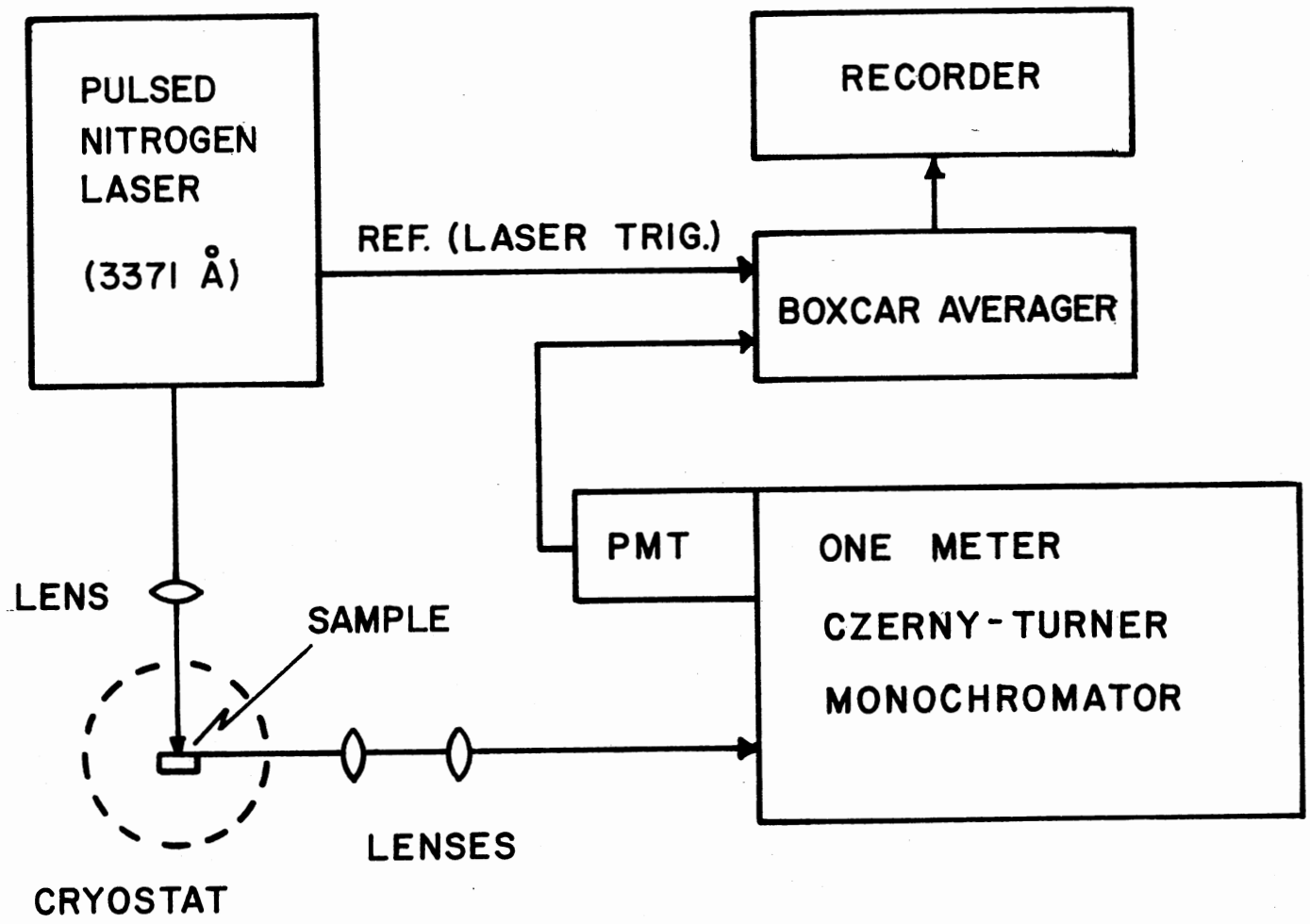

Figure 2. Block Diagram of the Time-Resolved Spectroscopy System

refrigerator system. An Avco-Everett Model C400 N_2 gas laser, with peak power of 20KW and half-width of 10ns was used in these experiments. The laser pulse rate was nominally about about 10pps. The sample fluorescence was analyzed by a one meter Spex Czerny-Turner monochromator, capable of $4x10^{-2}$ Å resolution in first order, and detected by a thermo-electrically cooled RCA C31034 photomultiplier tube. The phototube signal was processed by a Princeton Applied Research Model 162/164 boxcar averager triggered by the laser pulse and having a time resolution capability of 75ns. The signal was then subsequently recorded. Corning Glass CS 0-51 and CS 0-52 filters were placed at the slits of the monochromator to minimize the effects of scattered light from the laser. Using this set-up emission and lifetime data were taken for the undoped $CaWO_4$ sample, while both host and activator fluorescence intensities versus time, and lifetimes versus temperature measurements were performed on the doped samples.

The experimental set-up of the emission and excitation system is shown in Figure 3. Light from a Sylvania DXW 1000 watt tungsten-halogen lamp was passed through a Spex Minimate (0.22 meter Czerny Turner mount) monochromator and focused onto the sample, which was mounted to the cold-end of the refrigerator system. The grating blaze for this monochromator was 3000 Å. The sample emission was chopped at 104Hz by a Princeton Applied Research Model 125 mechanical light chopper and subsequently focused onto the entrance slits of a Jarrell-Ash Model 82-410 Ebert Monochromator. The grating in the Jarrell-Ash unit was blazed at 6000 Å. The analyzed signal was detected by a cooled RCA C 31034 photomultiplier which was interfaced

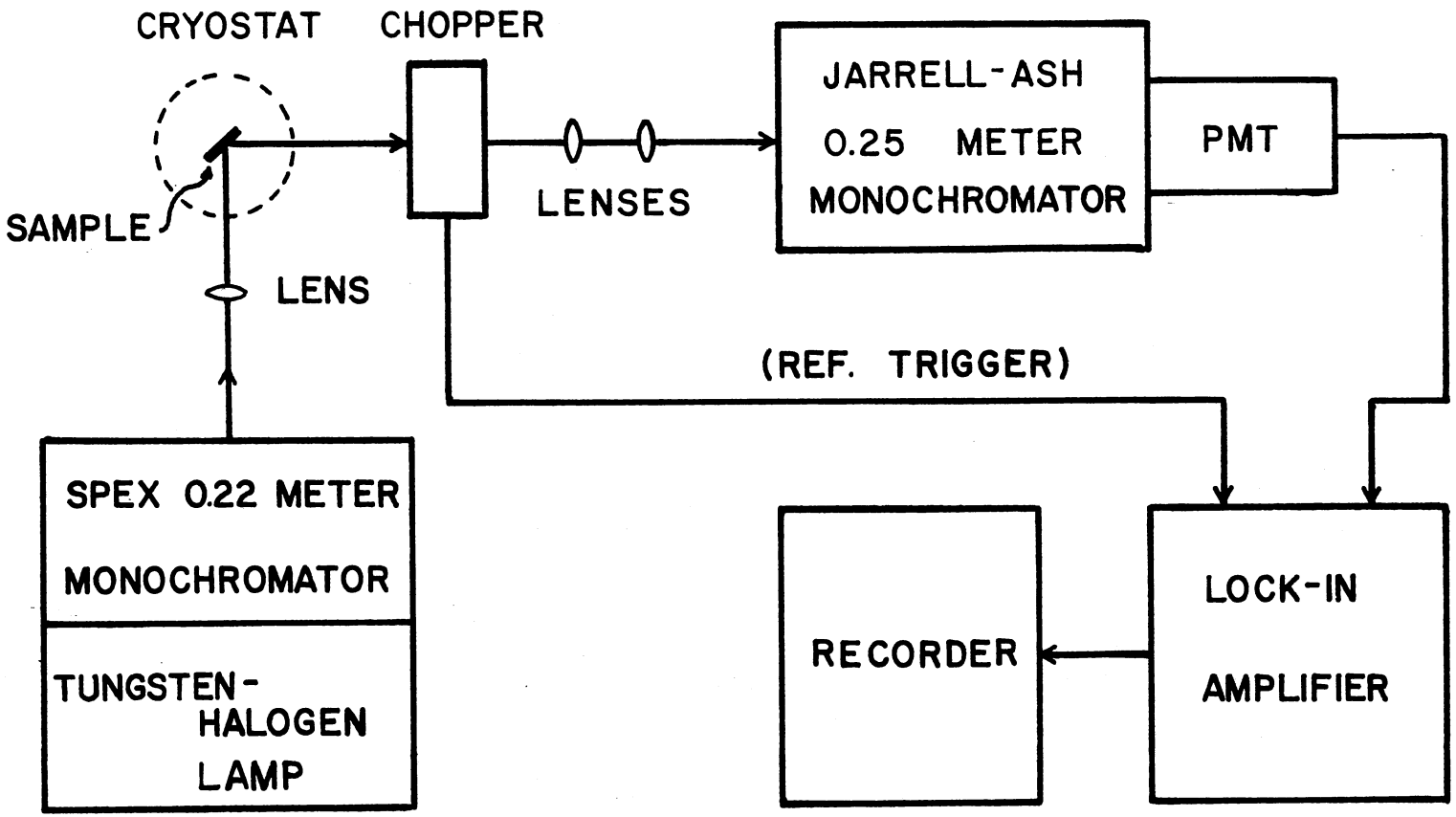

Figure 3. Block Diagram of the Excitation and Emission System

with the exit slits of the Jarrell-Ash monochromator. The phototube signal was processed by a Princeton Applied Research Model 128 lock-in amplifier having an internal narrow band pass filter with peak transmission at 100Hz. The chopper provided the reference trigger to the lock-in amplifier. The spectra were recorded on a strip chart recorder.

Emission spectra were obtained by placing the Spex monochromator on zero order and scanning the Jarrell-Ash. Excitation spectra were obtained by fixing the Jarrell-Ash to the specified emission wavelength and scanning the Spex. During emission runs a Corning Glass CS 4-94 filter was placed on the exit slit of the Spex and a CS 2-58 on the entrance slit of the Jarrell-Ash in order to limit the effects of scattered light. During excitation runs the CS 4-94 was removed. The phase settings used were those where emission signal was maximum. The monochromators used in emission and excitation were capable of about 200 Å resolution. The $MgO:Cr^{3+}$ excitation data were obtained from Henry (25).

The photoacoustic cell used was made of solid, polished aluminum, cylindrical in shape, following the design of Dr. R. C. Powell, as in Figure 4. A quartz entrance window and a quartz backing piece were sealed into the two flat ends of the cell and the microphone, with O-ring seal was placed on one side of the cylinder perpendicular to the cylindrical axis. A piece of heavy aluminum foil with a one millimeter aperture in the center was used to cover the microphone to exclude scattered light. A General Radio 1961 one inch electret microphone with a G. R. 1972-9600 preamplifier/adapter was used driven by a General Radio 1562-P60 power supply.

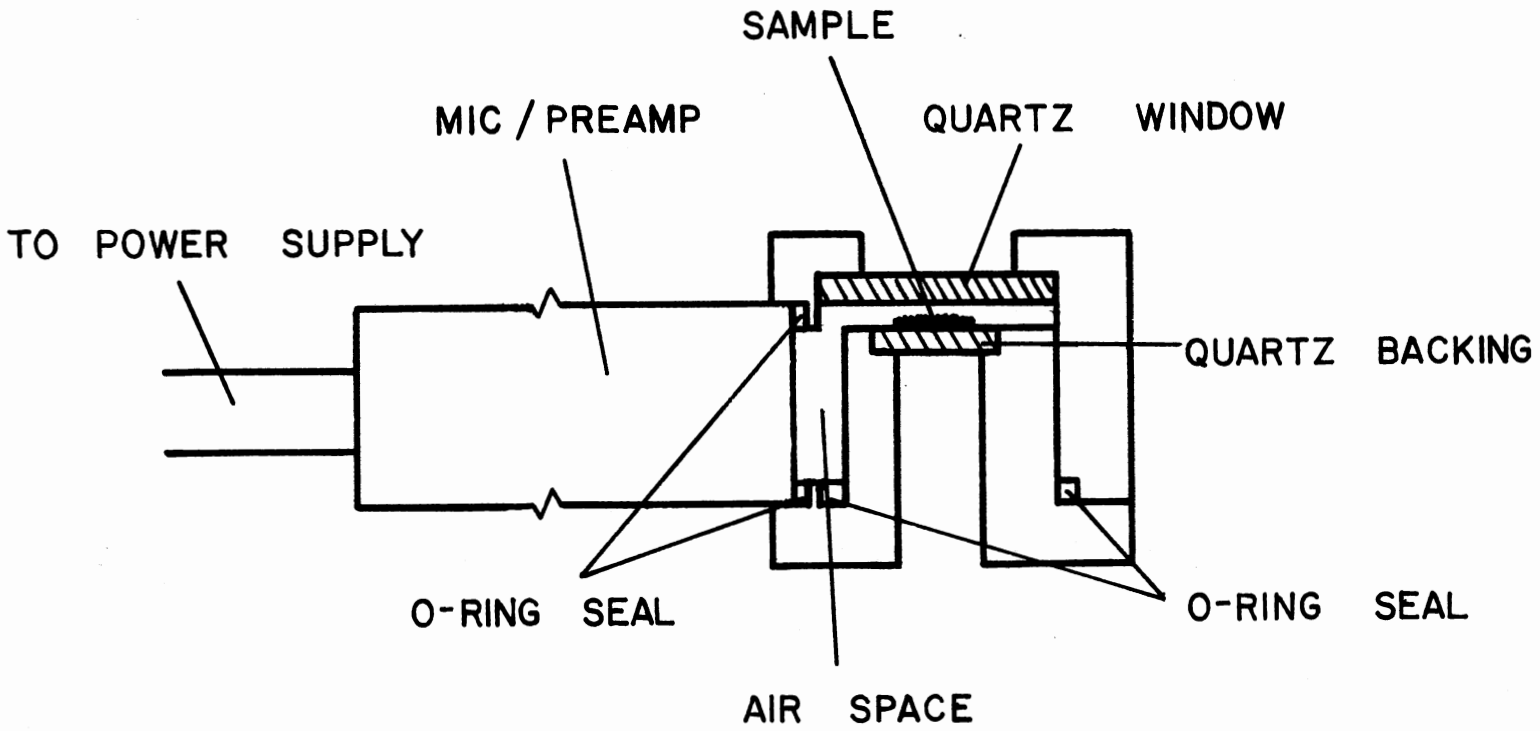

Figure 4. Cross Sectional View of the Photoacoustic Cell Designed by Dr. R. C. Powell

A block diagram of the photoacoustic spectrometer is shown in Figure 5. Light from the 1000 watt-tungsten halogen source was dispersed by passing it through the Spex Minimate monochromator. The light leaving the exit slit of the monochromator was then chopped at 104Hz and focused onto the sample contained within the photoacoustic cell. The signal from the microphone was amplified using a Princeton Applied Research Model 115 wide-band preamplifier and processed using the PAR Model 128 lock-in amplifier. When determining signal phases, the output was recorded on a strip chart. During spectral runs the signals were averaged using a Nicolet Model 1070 signal averager, where five scans were taken of each sample.

PAS peak phases were determined by finding the minimum in phase and adding 90°. The resolution of the system was 200 Å. Scanning speeds and instrument time constants were determined so as to avoid misrepresentation of the data while still achieving a good signal to noise ratio.

Correction for system response was accomplished by dividing the rough data point-by-point by a PAS spectrum of charcoal, a near-perfect blackbody absorber. This normalization procedure was applied to all PAS spectra as well as all excitation spectra except the $MgO:Cr^{3+}$ excitation spectrum obtained from Henry (25). The latter had already been normalized to system response. It had also been corrected for the energy dependence of the normalization curve, but this correction was lifted for use in the calculations which follow in Chapter V.

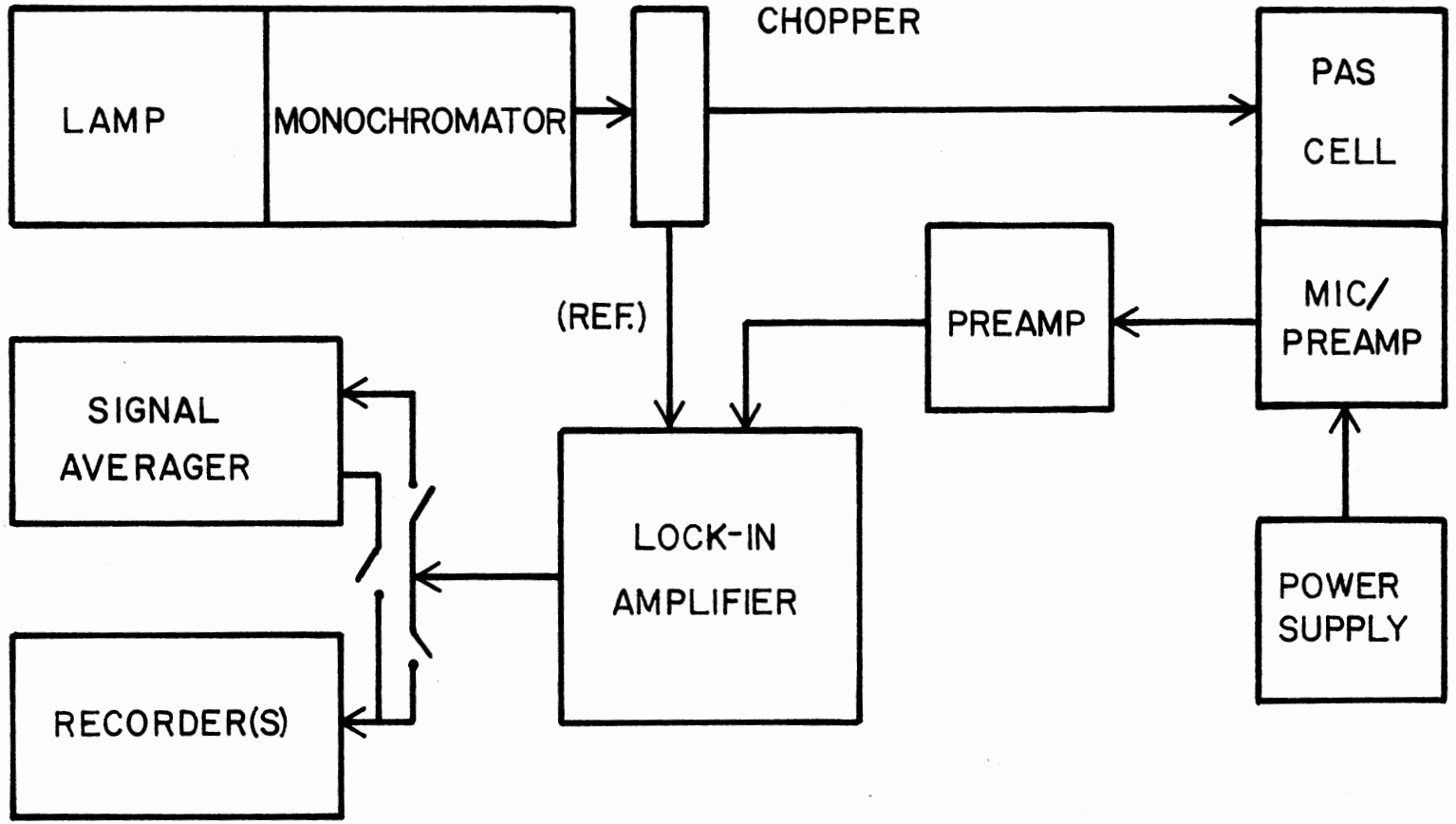

Figure 5. Block Diagram of the Photoacoustic Spectrometer

CHAPTER IV

HOST-SENSITIZED ENERGY TRANSFER IN $CaWO_4:Sm^{3+}$ AND $CaWO_4:Eu^{3+}$

Experimental Results

The absorption spectrum of undoped calcium tungstate is shown in Figure 6. The long wavelength tail of the absorption beginning at 3000 Å is of particular interest in this investigation. As indicated by the arrow, the laser excites the calcium tungstate crystals in this tail at 3371 Å. The sharp rise in the absorption below 3000 Å is the low energy edge of higher lying absorption bands which belong to various excited levels of the tungstate molecular ions (4).

Figure 7 shows the room temperature fluorescence spectra of $CaWO_4:Sm^{3+}$ which was observed at times of 0.8 μs after the laser pulse. The intrinsic host fluorescence gives rise to the broad band centered at 4500 Å. The typical sharp line fluorescence of the rare earths is seen at higher wavelengths arising from transitions between the $^4F_{5/2}$ level and the various levels of the ^6H_J manifold of the samarium ions (3).

Figure 8 shows the $CaWO_4:Sm^{3+}$ fluorescence spectra observed at 14K for times of 0.2 μs and 1.6 μs after laser excitation. It appears that some of the higher energy samarium transitions do not occur as readily at this temperature. In both Figures 7 and 8, the host

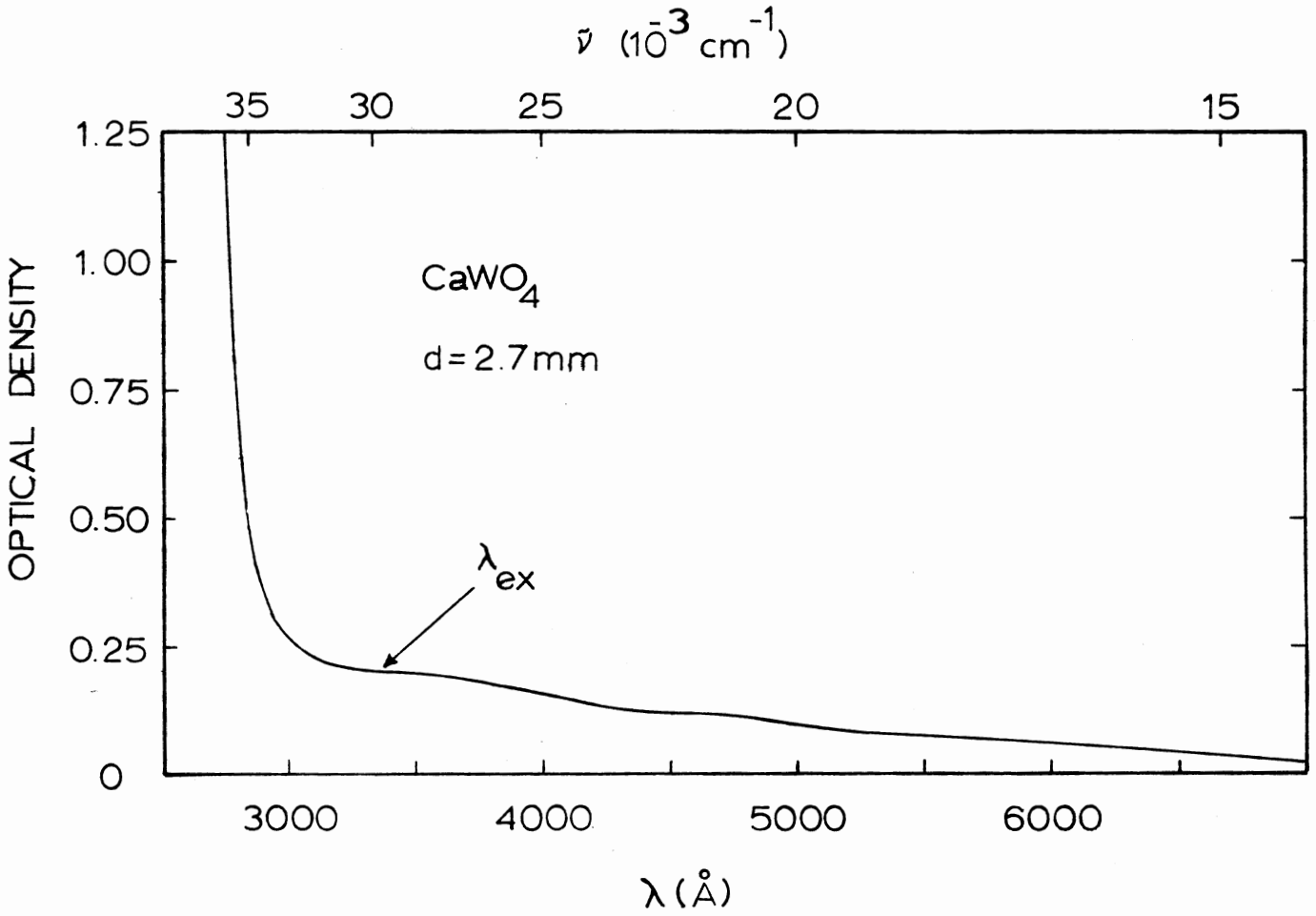

Figure 6. Absorption Spectrum of $CaWO_4$ at Room Temperature. Crystal Thickness is 2.8 mm. The Arrow Indicates the Wavelength of the Nitrogen Laser Excitation at 3371 Å

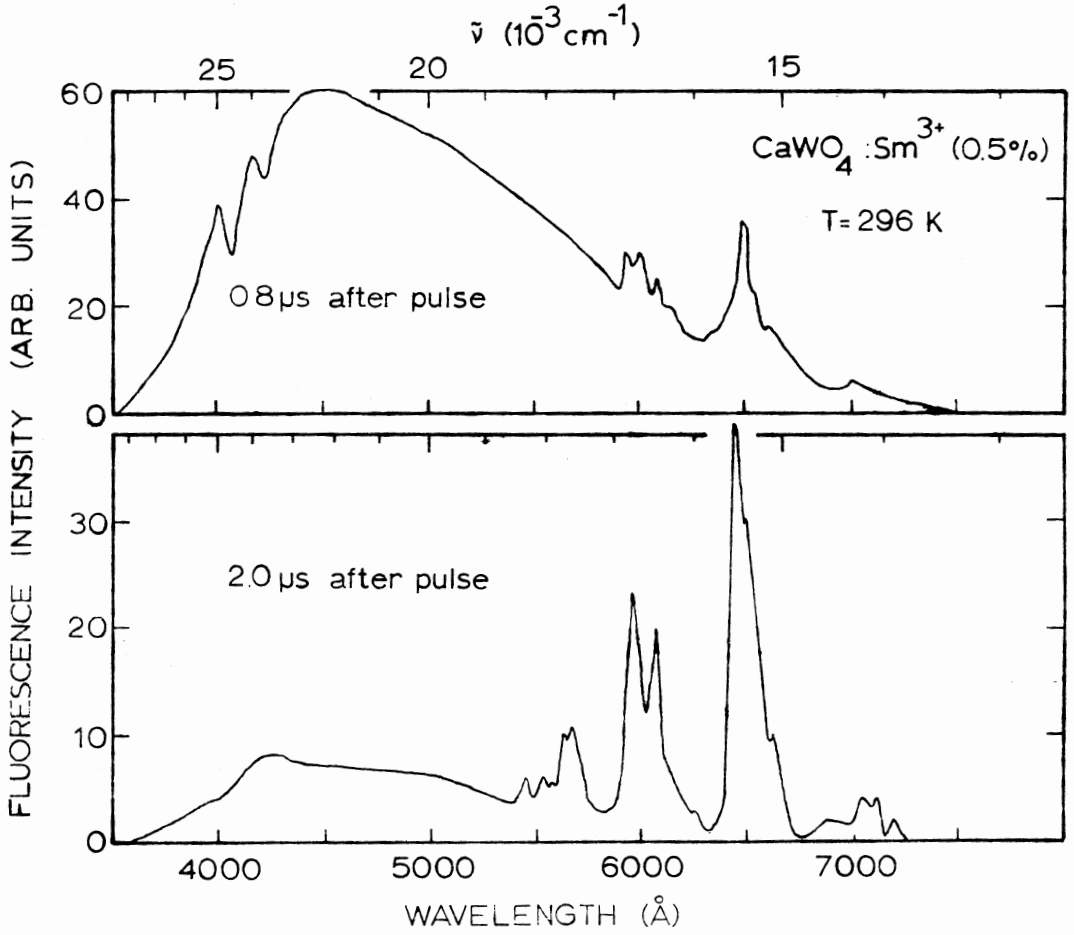

Figure 7. Fluorescence Spectra of $CaWO_4$:Sm^{3+} at Room Temperature, 0.8μs and 2.0μs After Laser Excitation

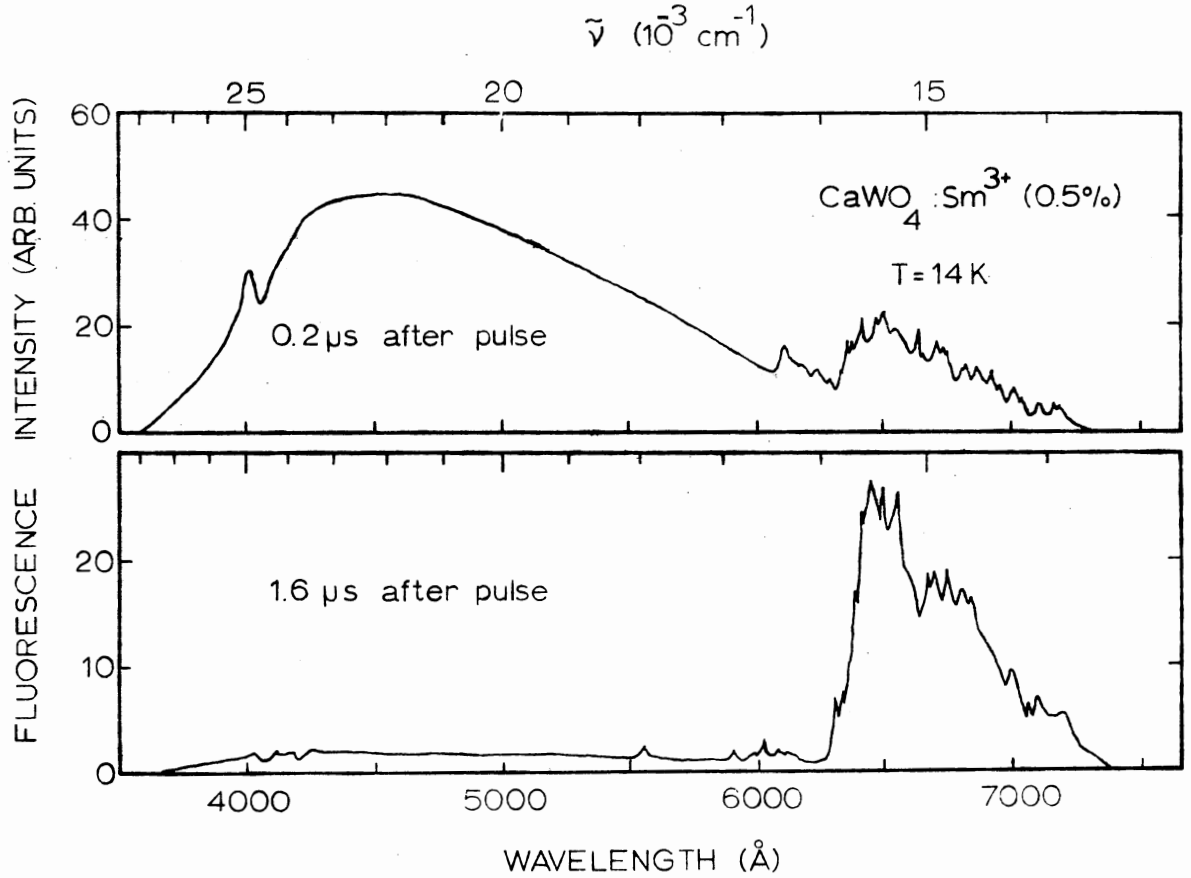

Figure 8. Fluorescence Spectra of $CaWO_4:Sm^{3+}$ at 14K, 0.2μs and 1.6μs After Laser Excitation

fluorescence intensity is seen to decrease in time while the samarium fluorescence increases. This is an indication that energy transfer is taking place between the excited tungstate molecular ions and the samarium activators.

Figure 9 shows the room temperature fluorescence spectra of $CaWO_4:Eu^{3+}$ at times of 0.3 μs and 1.0 μs after the laser pulse. Likewise, Figure 10 indicates the $CaWO_4:Eu^{3+}$ fluorescence spectra at 14K, 0.3 μs and 0.9 μs after excitation. The Eu^{3+} fluorescence is due to transitions from $^5D_1$, $^5D_0$, and possibly $^5D_2$ to ^7F_J levels (26). The host fluorescence intensity is again seen to decrease with time, with a subsequent rise in the intensity of the impurity fluorescence, indicating that energy transfer is taking place.

The results of the Time-Resolved Spectroscopy investigation of $CaWO_4:Sm^{3+}$ at room temperature and at 14K are tabulated in Tables I and II and shown in Figure 11. As is usual in TRS investigations the integrated fluorescence intensity of the activator, in this case the fluorescence intensity arising from the $^4F_{5/2}$ to $^6H_{9/2}$ samarium transition, is divided by the integrated host fluorescence intensity, and this ratio, I_A/I_S, is plotted as a function of time after the laser pulse. Inspection of Figure 11 indicates that there appears to be greater energy transfer at low temperatures.

Tables III and IV show the results of the TRS investigation of $CaWO_4:Eu^{3+}$ conducted at room temperature and at 14K. These results are shown in Figure 12. In the case of the europium doped sample, typical fluorescence intensities from $^5D_1$ and $^5D_0$ to ^7F_J transitions can be investigated separately. The increases in the relative intensity ratios for $CaWO_4:Eu^{3+}$ are seen to be generally not as great as

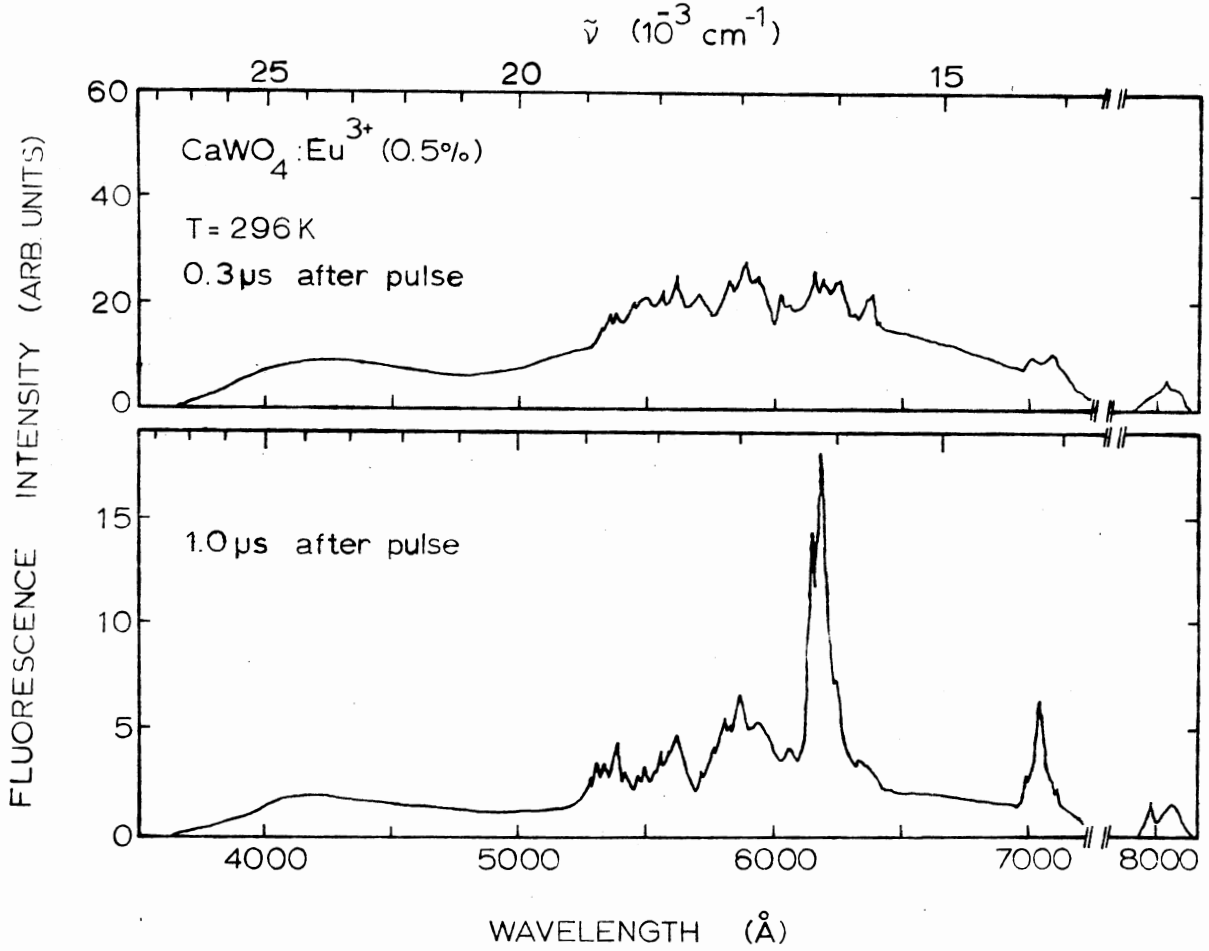

Figure 9. Fluorescence Spectra of $CaWO_4:Eu^{3+}$ at Room Temperature, 0.3μs and 1.0μs After the Pulse

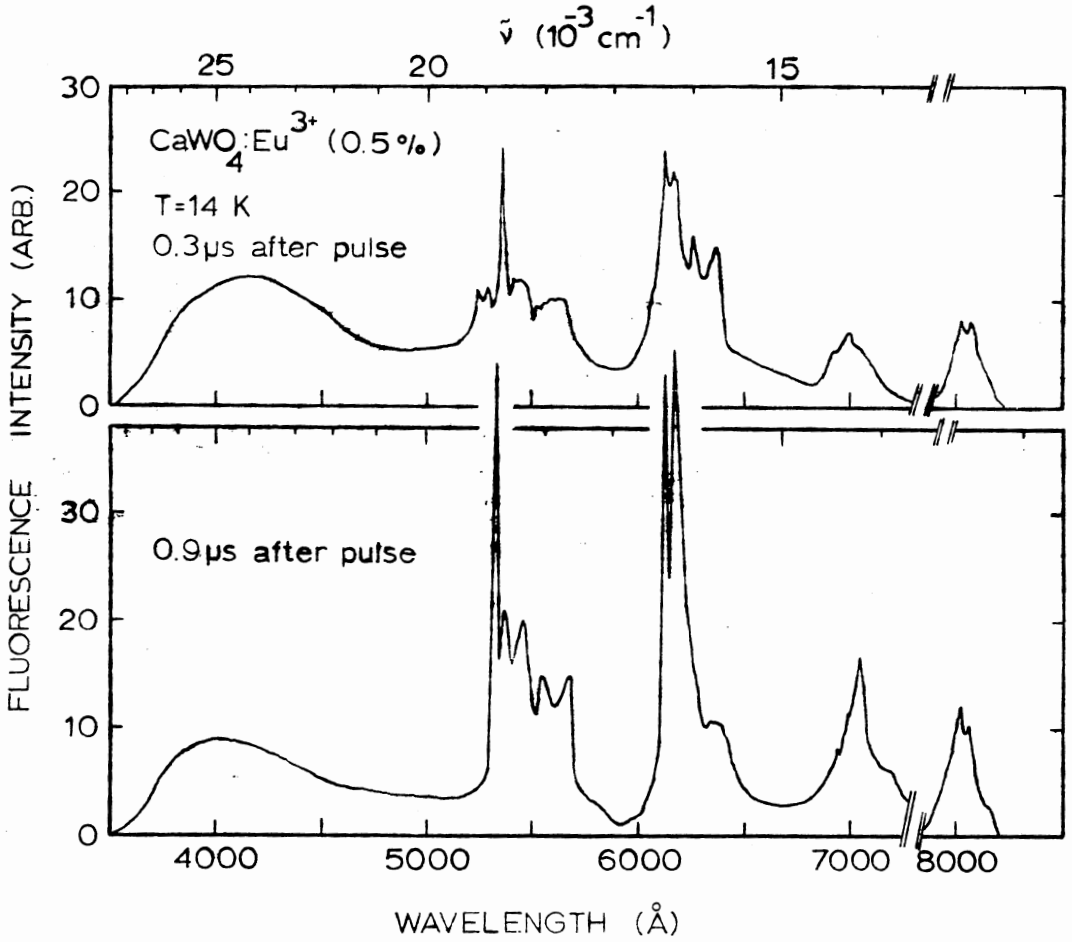

Figure 10. Fluorescence Spectra of $CaWO_4:Eu^{3+}$ at 14K, 0.3μs and 0.9μs After the Laser Pulse

TABLE I

TIME-RESOLVED SPECTROSCOPY RESULTS FOR
$CaWO_4:Sm^{3+}$ AT 296K*

Time After Pulse (μs)	Integrated Host Fluorescence Intensity, I_S (arb. units)	Integrated Impurity Fluorescence Intensity, I_A (arb. units)	$\frac{I_A}{I_S}$
0.2	8830	162	0.0183
0.5	5145	187	0.0363
0.8	6711	339	0.0505
1.0	3617	737	0.204
1.2	2355	630	0.268
1.4	2030	797	0.393
1.7	1331	660	0.496
2.0	686	842	1.23

* Sm^{3+} $^4F_{5/2}$ to $^6H_{9/2}$ transition monitored.

TABLE II

TIME-RESOLVED SPECTROSCOPY RESULTS FOR
$CaWO_4:Sm^{3+}$ AT 14K*

Time After Pulse (μs)	Integrated Host Fluorescence Intensity, I_S (arb. units)	Integrated Impurity Fluorescence Intensity, I_A (arb. units)	$\frac{I_A}{I_S}$
0.2	6095	440	0.0722
0.5	7778	1012	0.130
0.8	4506	1495	0.332
1.2	955	1824	1.91
1.6	570	1962	3.44

* Sm^{3+} $^4F_{5/2}$ to $^6H_{9/2}$ transition monitored.

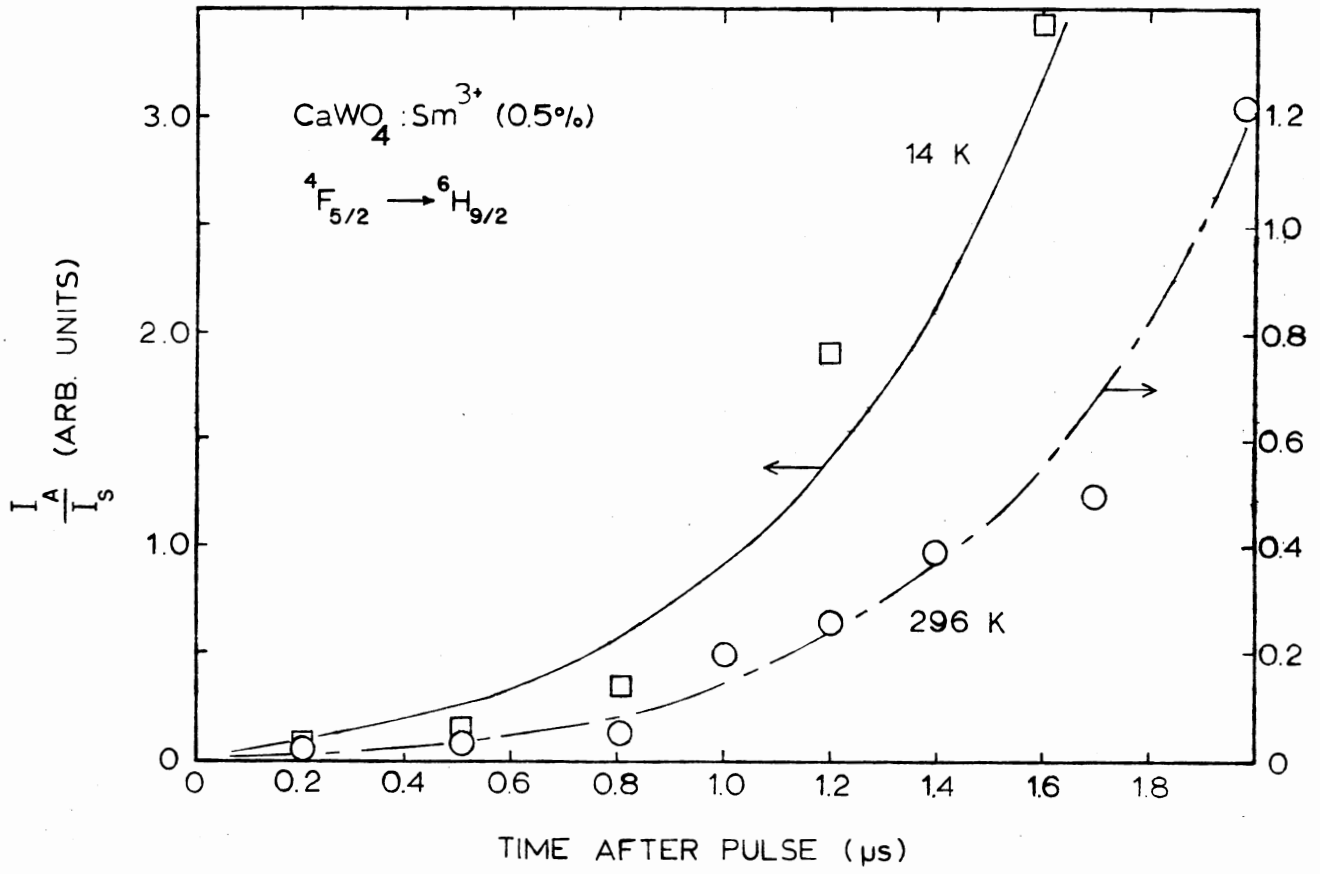

Figure 11. Time-Resolved Spectroscopy Results for $CaWO_4:Sm^{3+}$ at 296K and 14K. The $^4F_{5/2}$ to $^6H_{9/2}$ Transition is Monitored

TABLE III

TIME-RESOLVED SPECTROSCOPY RESULTS FOR
$CaWO_4:Eu^{3+}$ AT 296K

Time After Pulse (μs)	Integrated Host Fluorescence Intensity, I_S (arb. units)	Integrated Impurity $^5D_1$ Intensity, I_A^1 (arb. units)	Integrated Impurity $^5D_1$ Intensity, I_A° (arb. units)	$\frac{I_A^1}{I_S}$	$\frac{I_A^\circ}{I_S}$
0.1	5031	78	21	0.016	0.0042
0.3	3124	41	26	0.013	0.0083
0.5	5896	78	58	0.013	0.0098
0.8	2425	50	82	0.021	0.034
1.0	1784	70	117	0.039	0.066

TABLE IV

TIME-RESOLVED SPECTROSCOPY RESULTS FOR
$CaWO_4:Eu^{3+}$ AT 14K

Time After Pulse (μs)	Integrated Host Fluorescence Intensity, I_S (arb. units)	Integrated Impurity $^5D_1$ Intensity, I_A^1 (arb. units)	Integrated Impurity ^5D_o Intensity I_A° (arb. units)	$\frac{I_A^1}{I_S}$	$\frac{I_A^\circ}{I_S}$
0.1	2649	74	30	0.028	0.011
0.3	1577	80	39	0.051	0.025
0.5	2081	140	50	0.067	0.024
0.7	828	79	40	0.095	0.048
0.9	1315	176	74	0.13	0.056

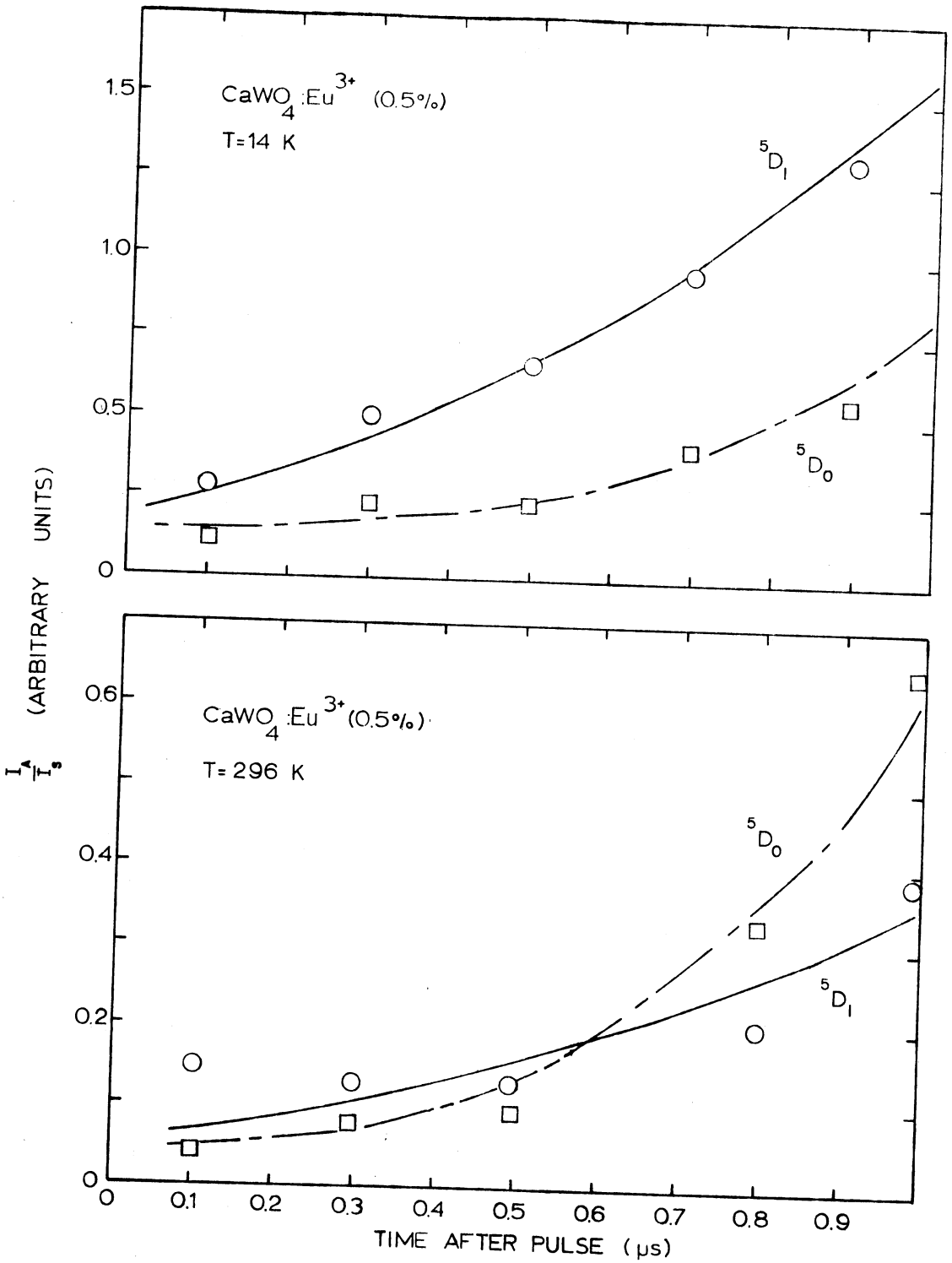

Figure 12. Time-Resolved Spectroscopy Results for $CaWO_4:Eu^{3+}$ at 296K and 14K. Both $^5D_0$ and $^5D_1$ to ^7F_J Transitions are Monitored

they are in $CaWO_4:Sm^{3+}$, but again there seems to be more energy transfer at low temperatures.

The fluorescence lifetimes for host and activator transitions are listed in Table V and shown in Figures 13 and 14 as a function of temperature. The undoped sample host fluorescence does not change with temperature generally, and on an average measures about 1.2 μs. This same lifetime is lowered to about 0.52 μs in $CaWO_4:Sm^{3+}$ and remains independent of temperature. Similar results occur in $CaWO_4:Eu^{3+}$, where the host lifetime measures approximately 0.62 μs for temperature between 14K and 296K. The samarium $^4F_{5/2}$ to $^6H_{9/2}$ transition fluorescence lifetime increases slightly with temperature, measuring 715 μs at 14K and 808 μs at room temperature. The lifetimes of the two europium transitions apparently decrease with increasing temperature with the ^5D_o to ^7F_J transition lifetime measuring 535 μs at 14K and 338 μs at 296K. The $^5D_1$ to ^7F_J transition lifetime measures about 4.0 μs at 14K and 1.3 μs at 250K.

Interpretation of Results

The model used to interpret the results of the TRS investigation and lifetime measurements of $CaWO_4:Sm^{3+}$ is shown in Figure 15. The concentration of host tungstate ions is represented by n_x. The fluorescence decay rate of the ions comprising n_x is given by β_x. Similarly, the concentration of excited activators is expressed by n_A. Fluorescence decay of these ions occurs at a rate β_A. Initial excitation of level n_x is represented by W, and the energy transfer occurs at a rate given by ω. The changes with time of concentrations n_x and n_A are given by the rate equations, which are expressed as

TABLE V

FLUORESCENCE LIFETIMES (μs) AT VARIOUS TEMPERATURES FOR OBSERVED TRANSITIONS IN $CaWO_4$, $CaWO_4:Sm^{3+}$, $CaWO_4:Eu^{3+}$

Sample	Temperature (K)*							
	14K	20K	33K	68K	97K	171K	251K	296K
$CaWO_4$								
Host	1.34	--	--	--	--	--	--	1.04
$CaWO_4:Sm^{3+}$								
Host	0.50	0.53	0.53	0.53	0.47	0.53	0.52	0.52
$^4F_{5/2}$ to $^6H_{9/2}$	715	780	--	727	820	819	784	808
$CaWO_4:Eu^{3+}$								
Host	0.58	0.68	0.55	0.64	0.63	0.69	0.52	0.66
^5D_o to ^7F_J	535	600	530	487	515	425	439	338
$^5D_1$ to ^7F_J	4.05	--	4.2	4.3**	4.2	--	1.3	--

* Temperatures above 68K are ± 5K
** Average value

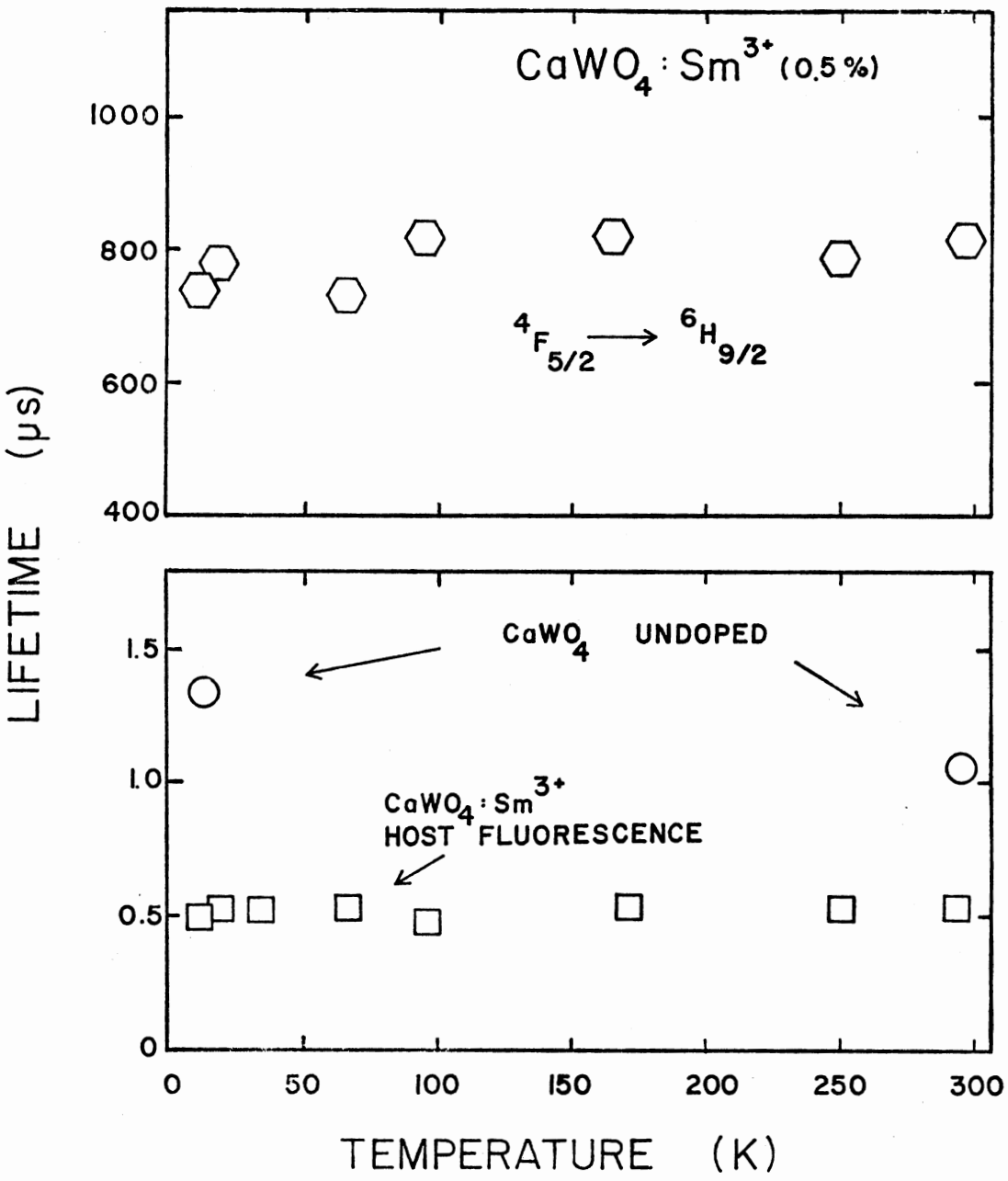

Figure 13. Temperature Dependence of the Fluorescence Lifetimes of the Undoped $CaWO_4$ and $CaWO_4:Sm^{3+}$ Host Fluorescence (Below) and the $CaWO_4:Sm^{3+}$ $^4F_{5/2}$ to $^6H_{9/2}$ Transition (Above)

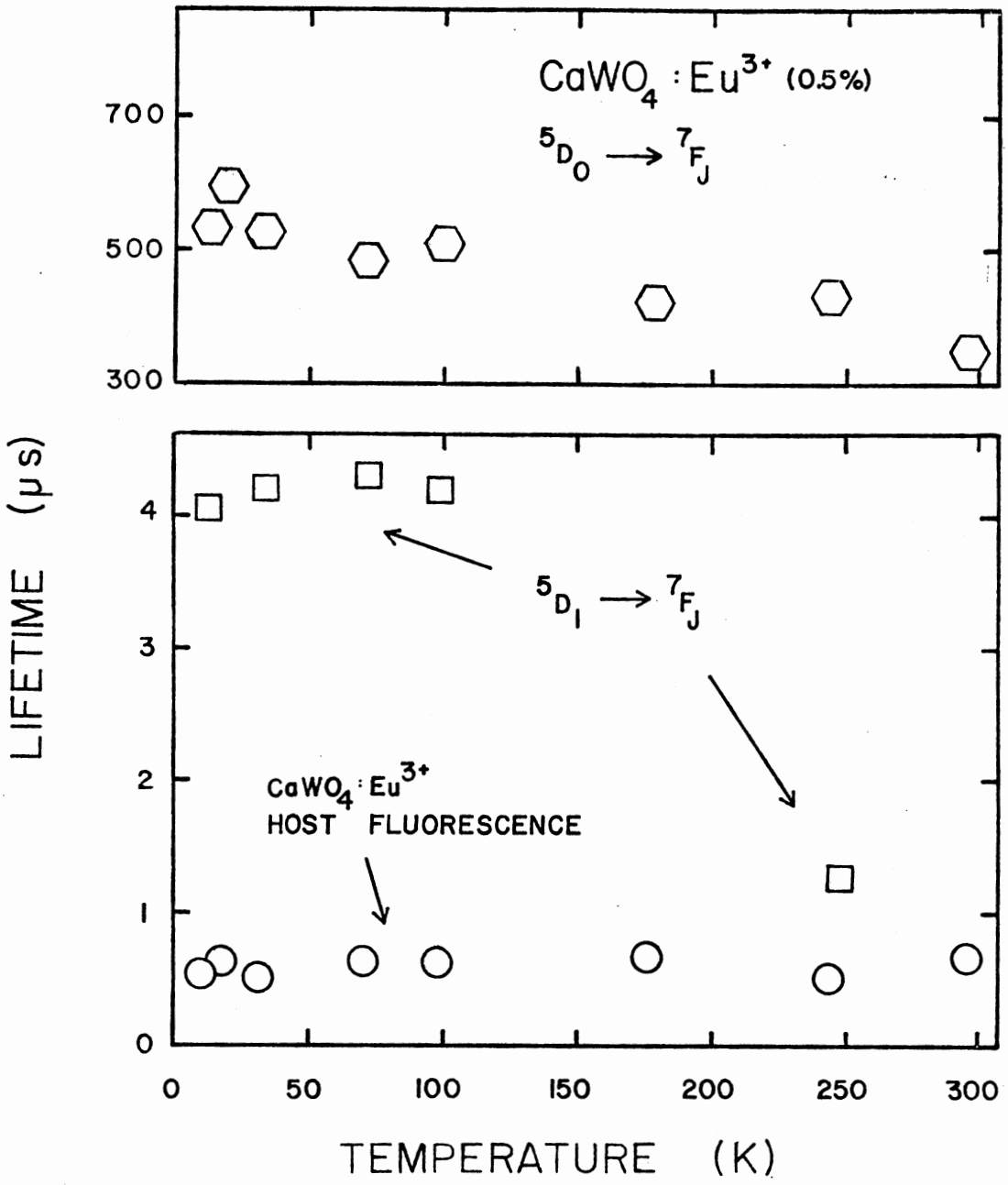

Figure 14. Temperature Dependence of the Fluorescence Lifetimes of the Host Fluorescence and $^5D_1$ to ^7F_J Transition in $CaWO_4:Eu^{3+}$ (Below) and the $^5D_0$ to ^7F_J Transition (Above)

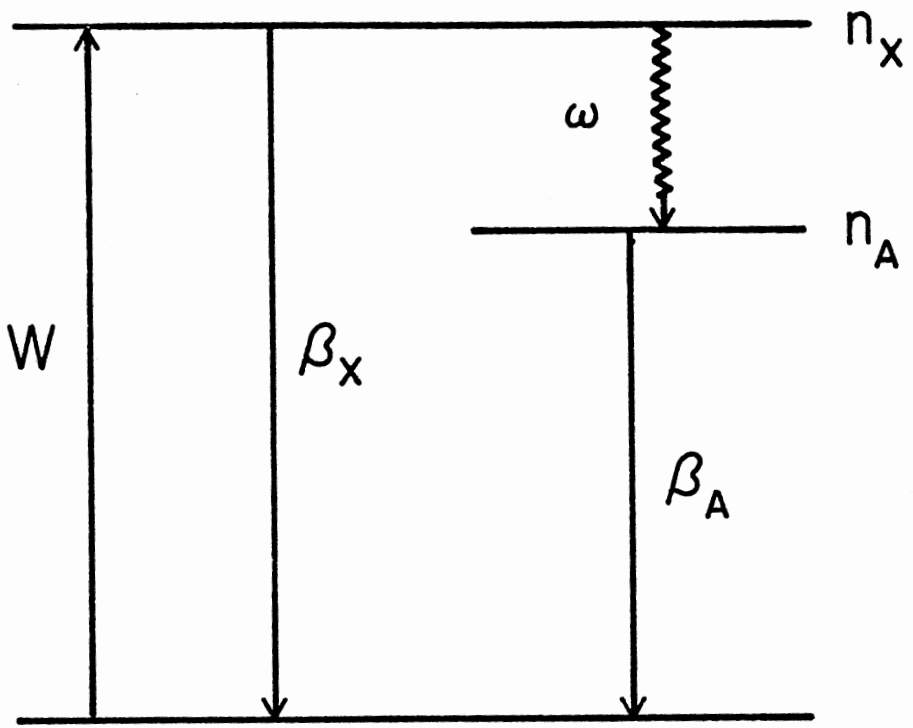

Figure 15. Proposed Model for Interpreting the Results of Time-Resolved Spectroscopy and Lifetime Measurements of $CaWO_4:Sm^{3+}$

$$dn_x/dt = W - (\beta_x+\omega)n_x \qquad (54)$$

and

$$dn_A/dt = \omega n_x - \beta_A n_A \qquad (55)$$

Solutions to these two equations can be obtained by considering W to be a delta function in time and ω to be independent of time. These solutions can then be expressed as a ratio which is proportional to the ratio of integrated fluorescence intensities determined previously. Thus,

$$I_A/I_S \propto n_A/n_x = \omega\,[(\beta_x+\omega)-\beta_A]^{-1}\left\{\exp\,[(\beta_x+\omega-\beta_A)t] - 1\right\} \qquad (56)$$

Using ω as an adjustable parameter and substituting the measured experimental values into Equation (56), curves are generated which represent accurate fits of the above model to the experimental data. These curves are shown as the lines in Figure 11.

The model used to interpret the results from the investigation of $CaWO_4:Eu^{3+}$ is shown in Figure 16. n_A^o and n_A^1 represent the concentrations of excited activator ions from levels ^5D_o and $^5D_1$. The decay rates for these ions are given by β_A^o and β_A^1. The absorption and emission of phonons between the levels is represented by γ_1 and γ_2, where

$$\gamma_2 = \gamma_1 \,/\, \exp\,(\Delta E_{10}/kT)\ . \qquad (57)$$

All other designations are the same as previously given. The changes with time of the various concentrations are again given by the rate equations, which are expressed as

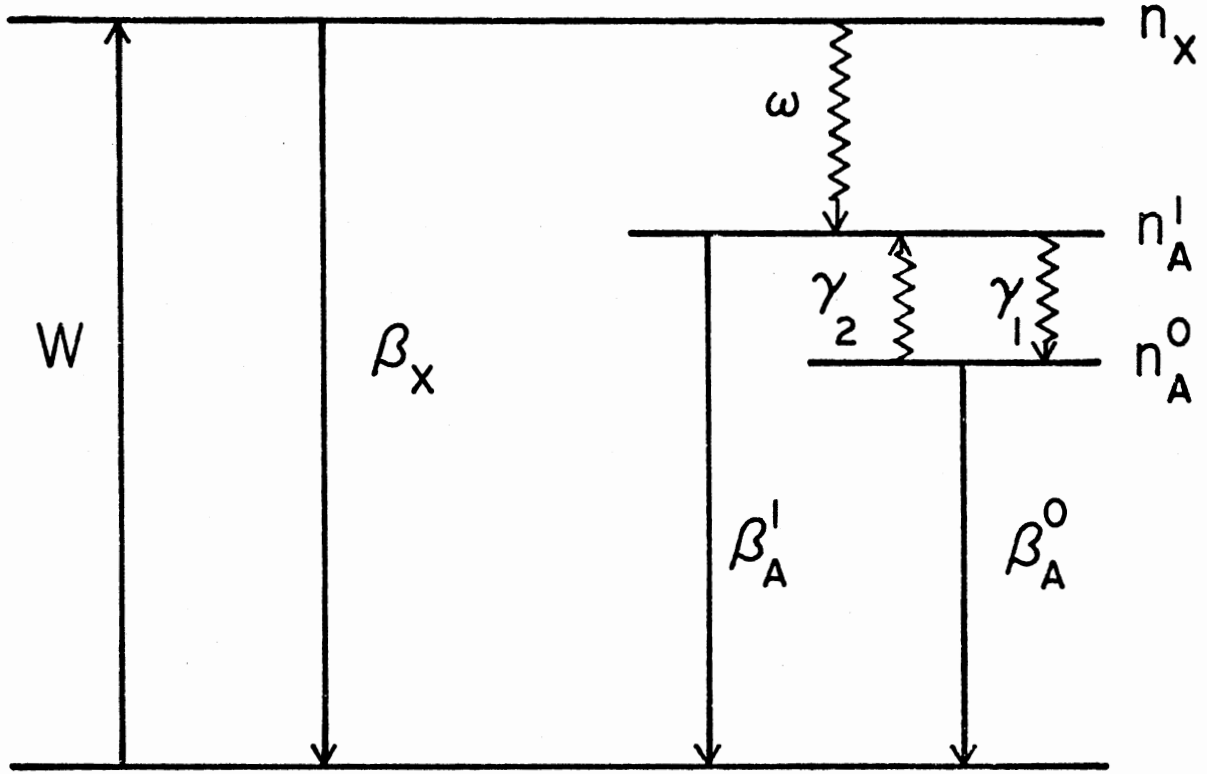

Figure 16. Proposed Model for Interpreting the Results of Time-Resolved Spectroscopy and Lifetime Measurements of $CaWO_4:Eu^{3+}$

$$dn_x/dt = W - (\beta_x+\omega)n_x \tag{58}$$

$$dn_A^1/dt = \gamma_2 n_A^\circ - (\gamma_1+\beta_A^1)n_A^1 + \omega n_x \tag{59}$$

and

$$dn_A^\circ/dt = \gamma_1 n_A^1 - (\gamma_2+\beta_A^\circ)n_A^\circ \tag{60}$$

Solutions to these equations can be obtained by again considering W to be a delta function in time and ω to be independent of time. Forming ratios of these solutions yields expressions which are proportional to the ratios of integrated fluorescence intensities, which can be written as.

$$I_A^\circ/I_S \propto n_A^\circ/n_x = \gamma_1\omega \left\{ \frac{1}{(\beta_x+\omega+p_1)(\beta_x+\omega+p_2)} + \frac{\exp[(\beta_x+\omega+p_1)t]}{(\beta_x+\omega+p_1)(p_1-p_2)} - \frac{\exp[(\beta_x+\omega+p_2)t]}{(\beta_x+\omega+p_2)(p_1-p_2)} \right\} \tag{61}$$

and,

$$I_A^1/I_S \propto n_A^1/n_x = \omega \left\{ \frac{-\beta_x - \omega + \gamma_2 + \beta_A^\circ}{(\beta_x+\omega+p_1)(\beta_x+\omega+p_2)} + \frac{(p_1+\gamma_2+\beta_A^\circ)\exp[(\beta_x+\omega+p_1)t]}{(\beta_x+\omega+p_1)(p_1-p_2)} - \frac{(p_2+\gamma_2+\beta_A^\circ)\exp[(\beta_x+\omega+p_2)t]}{(\beta_x+\omega+p_2)(p_1-p_2)} \right\} \tag{62}$$

where

$$p_1 = \left\{ -(\gamma_2+\beta_A^\circ+\gamma_1+\beta_A^1) + [(\gamma_2+\beta_A^\circ-\gamma_1-\beta_A^1)^2 + 4\gamma_1\gamma_2]^{\frac{1}{2}} \right\}/2 \tag{63}$$

and

$$p_2 = \left\{ -(\gamma_2+\beta_A^{\circ}+\gamma_1+\beta_A^{1}) - [(\gamma_2+\beta_A^{\circ}-\gamma_1-\beta_A^{1})^2 + 4\gamma_1\gamma_2]^{\frac{1}{2}} \right\}/2 \qquad (64)$$

Using both ω and γ_1 as adjustable parameters, and substituting the experimentally measured values into Equations (61) and (62) yields the curves shown by the lines in Figure 12, which are accurate fits of the model to the experimental data.

Inspection of Figures 11 and 12 seem to indicate that more energy transfer is occurring at low temperatures, but host lifetime quenching calculations and the models used to interpret the results imply a constant energy transfer rate. This apparent discrepancy can be explained by the following: In fitting the experimental data through Equations (56), (61) and (62) use was made of multiplicative proportionality constants which do not appear in these equations. For the case of the Sm^{3+} work this constant decreases by a factor of about 6 between the solutions of the equation at 14K and those at 296K. The constant used in the Eu^{3+} $^5D_1$ work decreases by a factor of about 4 for the same temperature variation. The constant used in the Eu^{3+} $^5D_0$ work does not change for solutions of the equation at these two temperatures. These constants include the ratios of the quantum efficiencies of the host and activators ions involved in the energy transfer, and these ratios might be temperature dependent. Use was also made of an additive constant in the Eu^{3+} work to fit the solutions of Equations (61) and (62) to the data. The value of this constant is the same for both Eu^{3+} levels, and decreases by a factor of three for solutions at 14K versus 296K. This constant probably reflects the

importance of back transfer from the activators to the host, or perhaps of direct pumping of the Eu^{3+} ions.

The most probable mechanisms for energy transfer are electric dipole-dipole and exchange interaction. The energy transfer rate for the electric dipole-dipole case is given by Equation (17). Substituting the experimentally measured values into this equation yields values for the critical energy transfer distance, R_o, of 3.8 Å for Sm^{3+} and 3.6 Å for Eu^{3+}. R_o can also be theoretically predicted from the spectral overlap integral, (see Equation 17). The predicted value for Sm^{3+} is 4.0 Å (3), which is similar to the experimentally derived value. The predicted value for Eu^{3+}, however, is much larger than the experimentally derived value, measuring 16.2 Å. This predicted value was calculated using an index of refraction of 1.92 for $CaWO_4$, an average energy in the region of the overlap of 2.375×10^4 cm^{-1}, a sensitizer quantum efficiency of one and a spectral overlap of 1.35×10^2 ℓ/mole-cm, (see Figure 17 for a typical illustration). This large value for R_o may be the result of clustering in the Eu^{3+} ions instead of being uniformly distributed throughout the crystal. In this case an excited tungstate ion might transfer its energy to only one member of the neighboring cluster, (the transfer will be shown to be a nearest neighbor process below), with the remaining members not taking part in the transfer process.

The energy transfer rate by exchange interaction is given by Equation (21). Substituting the experimentally measured values into this equation and assuming L has a value equal to half the tungsten-oxygen separation distance, which is 0.9 Å, yields values for the

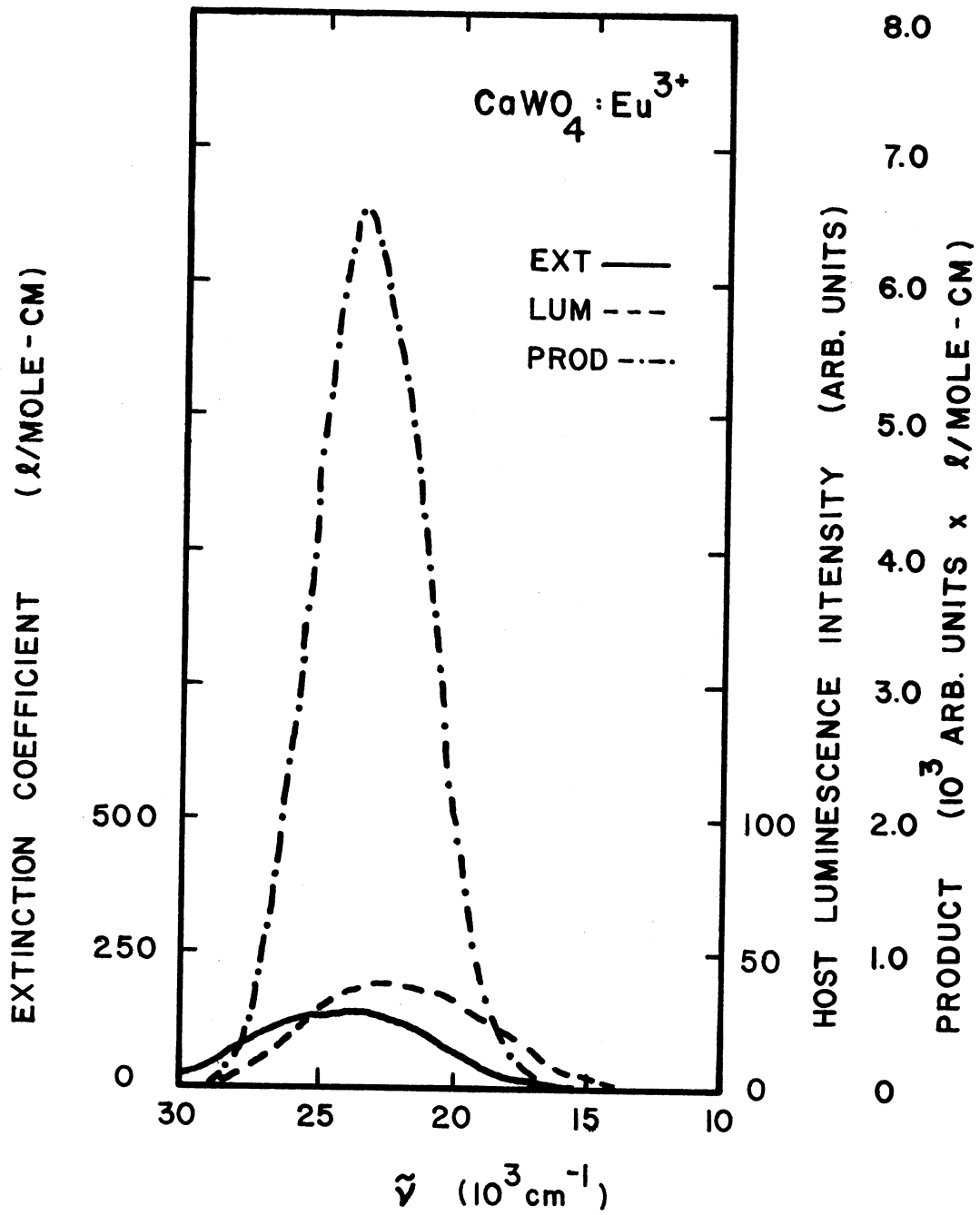

Figure 17. Illustration Indicating the Degree of Spectral Overlap in $CaWO_4:Eu^{3+}$

critical energy transfer distance, R_0', of 3.8 Å for Sm^{3+} and 3.6 Å for Eu^{3+}. A theoretical prediction of R_0' is not possible without knowledge of the wave function overlap, but the experimentally determined values seem acceptable.

The values of the energy transfer and relaxation parameters discussed above are shown in Table VI. The energy transfer rates shown are equivalent to those obtained by host fluorescence lifetime quenching. The rates in Table VI are significantly larger than those obtained for excitation into the major host absorption bands (3). The value of γ_1 shown approximates the rate reported in the literature (27). Since the energy transfer rate is found to be constant in time, it would seem that each tungstate ion transferring energy is surrounded by a similar environment. Also, the higher transfer rate observed here indicates that the energy transfer is taking place between these excited tungstate ions and their nearest neighbor activators. Thus it is concluded that absorption of excitation into the long wavelength tail of the $CaWO_4$ absorption band selectively excites tungstate ions which are nearest neighbors to activator impurities.

TABLE VI

ENERGY TRANSFER AND RELAXATION PARAMETERS

Parameter	$CaWO_4:Sm^{3+}$	$CaWO_4:Eu^{3+}$
ω(TRS)	1.1×10^6/sec	7.5×10^5/sec
R_o(EDD)		
experimental	3.8 Å	3.6 Å
predicted	4.0 Å	16.2 Å
R_o'(exch)		
experimental	3.8 Å	3.6 Å
Spectral Overlap	3.35×10^{-2} ℓ/mole-cm	1.35×10^2 ℓ/mole-cm
γ_1	--	1.1×10^5/sec

CHAPTER V

PHOTOACOUSTIC SPECTROSCOPY OF Cr^{3+} IONS IN VARIOUS HOST MATERIALS

The purpose of this chapter is to present the results of PAS experiments performed on $Al_2O_3:Cr^{3+}$, $MgO:Cr^{3+}$, $SrTiO_3:Cr^{3+}$ and $BaTiO_3:Cr^{3+}$, with a desire to try and elucidate the avenues of radiationless deexcitation of the chromium ions in these materials. Emphasis will be placed on the results from the two major chromium absorption bands, designated $^4T_1$ and $^4T_2$. The experimental results will be reported first, followed by a discussion of these results.

$Al_2O_3:Cr^{3+}$

Figures 18, 19 and 20 show the absorption, R line excitation and photoacoustic spectra of $Al_2O_3:Cr^{3+}$. The absorption data in Figure 18 are plotted as optical density versus wavelength from 2000 Å to 7000 Å. Notable features are the $^4T_1(e^2t)$ band at 2500 Å, the major $^4A_2 \rightarrow {}^4T_1(et^2)$ absorption band at 4000 Å, a possible $^2T_2(t^3)$ shoulder at about 4600 Å, the major $^4A_2 \rightarrow {}^4T_2(et^2)$ band at 5600 Å, and the small $^2E(t^3)$ band at about 6850 Å. As compared to the low temperature data reported by McClure (28), it appears that Figure 18 represents a mixture of polarizations both perpendicular and parallel to the C_3 axis. Relative peak heights indicate that the $^4T_1(et^2)$ peak is approximately twice the height of the $^4T_2(et^2)$ peak.

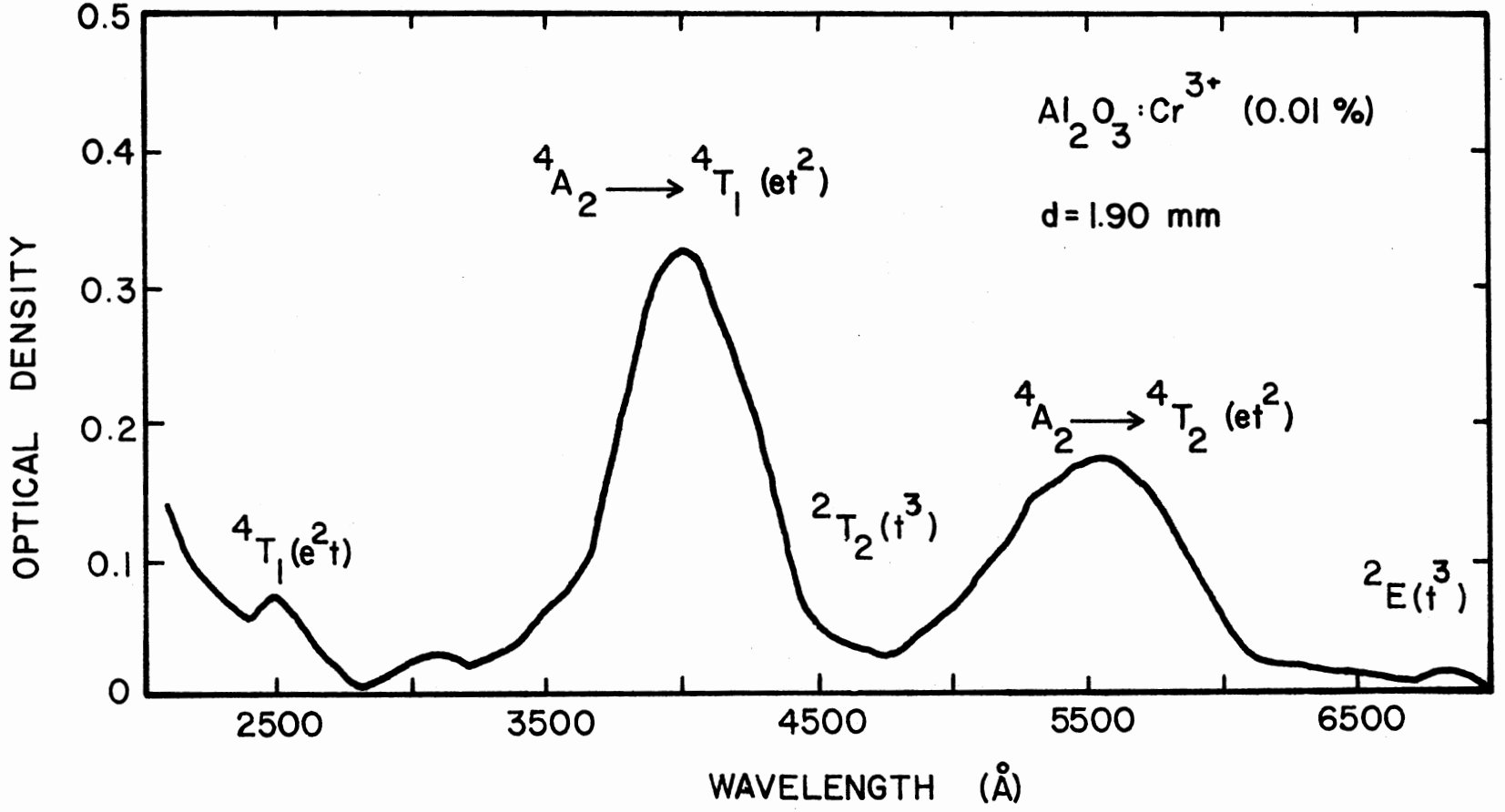

Figure 18. Room Temperature Absorption Spectrum of $Al_2O_3:Cr^{3+}$ (0.01%)

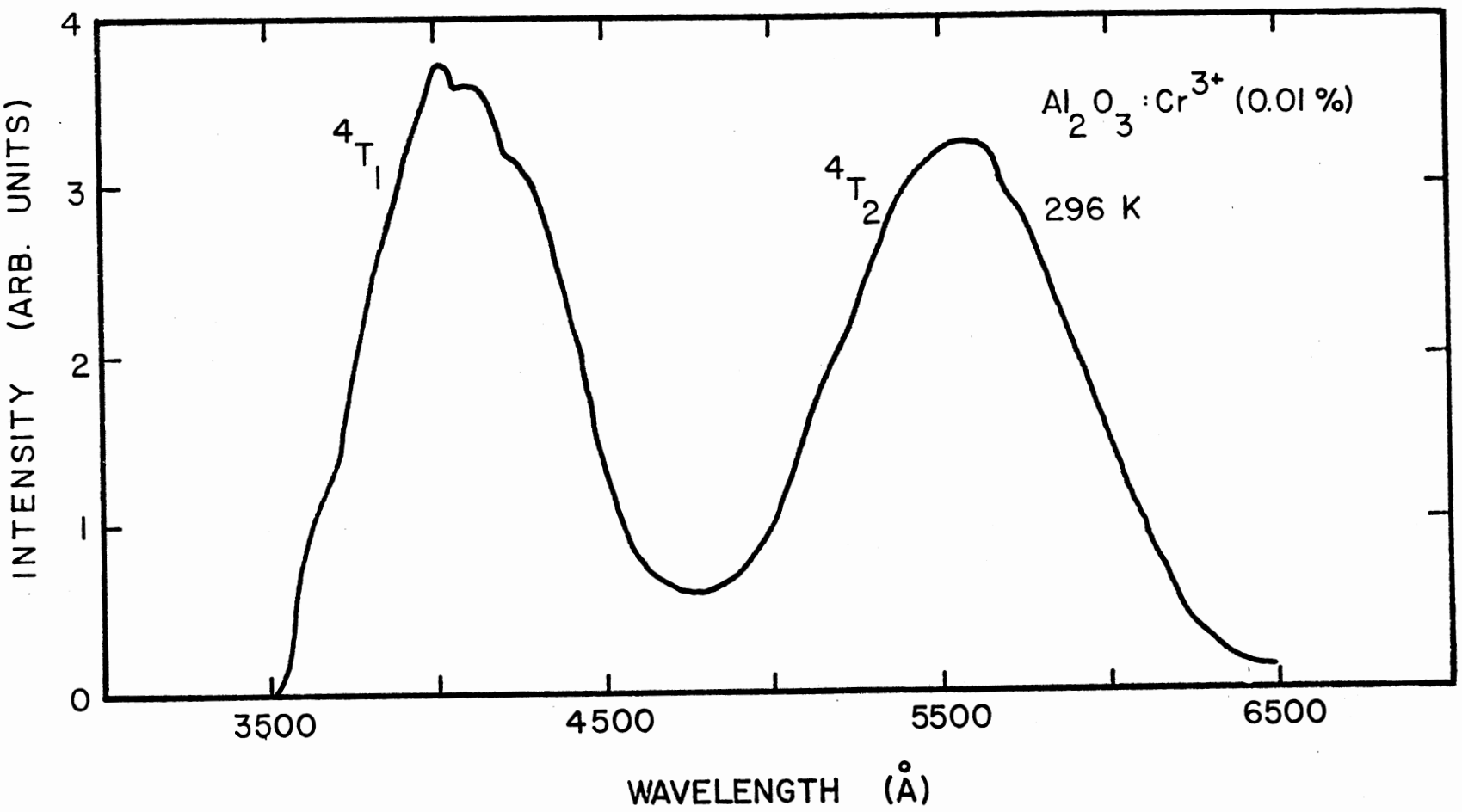

Figure 19. Normalized Room Temperature Excitation Spectrum of the R Lines of $Al_2O_3:Cr^{3+}$ (0.01%)

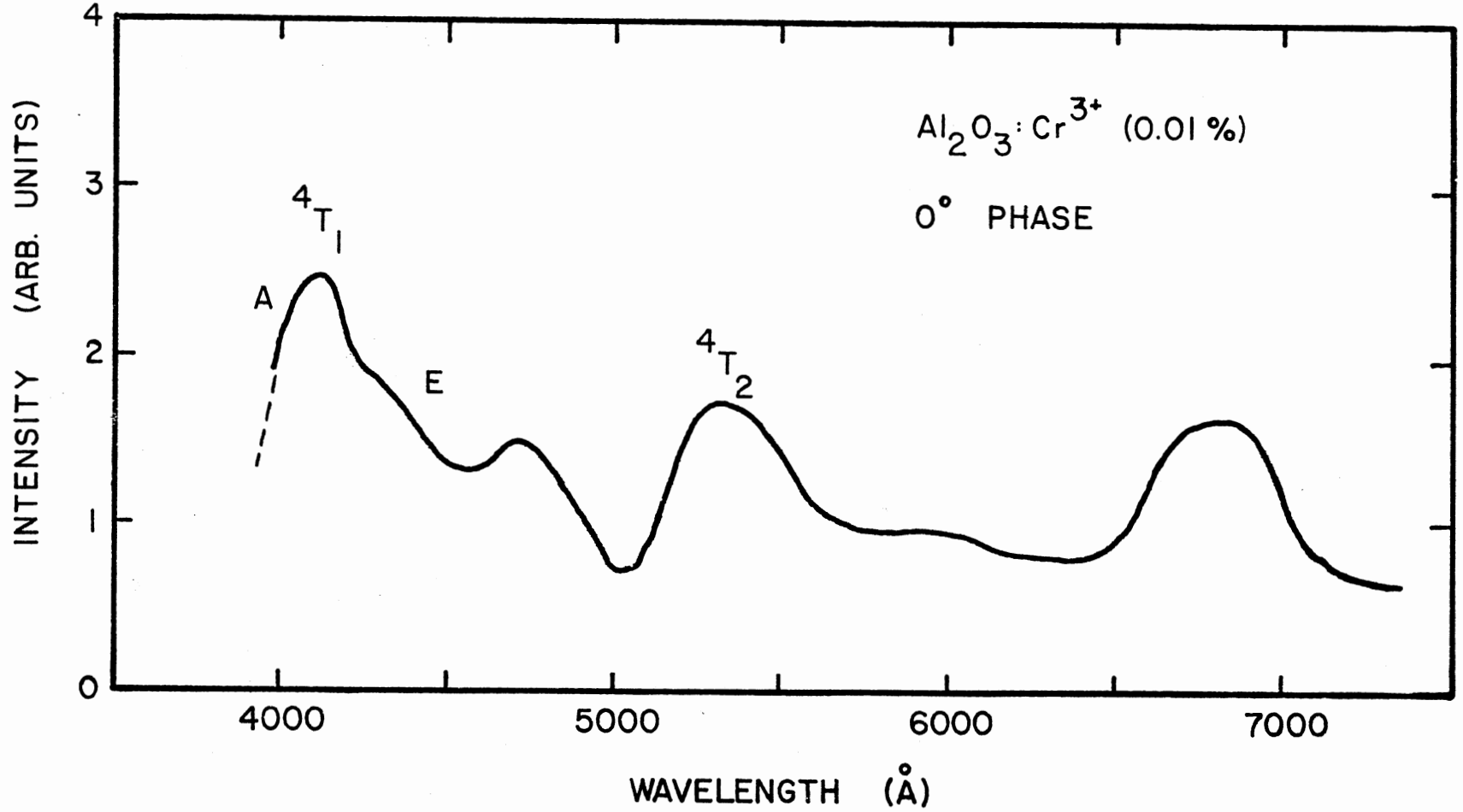

Figure 20. Normalized Room Temperature Photoacoustic Spectrum of $Al_2O_3:Cr^{3+}$ (0.01%)

Figure 19 shows the room temperature R line excitation spectrum plotted as arbitrary intensity units versus wavelength, from 3000 Å to 6500 Å. Two peaks appear, the $^4T_1$ peak at 4000 Å and the $^4T_2$ peak at 5600 Å. Relative peak heights show an almost one to one correspondence. For lightly doped ruby Powell (29) reports the $^4T_2$ peak to be twice the relative height of $^4T_1$ and observes that although this is opposite to what is seen in absorption, it is in accord with data reported by Misu (30) for perpendicularly polarized light. The data in Figure 19 undoubtedly reflect both polarizations in excitation.

The PAS spectrum in Figure 20 shows three major peaks at ca. 4100 Å, 5300 Å, and 6850 Å. These can be associated with the $^4T_1 \rightarrow {}^4A_2$, $^4T_2 \rightarrow {}^4A_2$ and possible $^2E \rightarrow {}^4A_2$ transitions respectively. A smaller band at 4700 Å appears which could possibly represent the $^2T_2(t^3)$ transition. The $^4T_1$ level is partially reduced into its A and E components, the E component being the shoulder at 4300 Å. These results compare favorably with the results reported by Murphy and Aamodt (5). Table VII lists the $^4T_1$ and $^4T_2$ integrated PAS intensities and their ratio as well as those in absorption and excitation for $Al_2O_3:Cr^{3+}$. All peaks monitored in the ruby PAS spectrum exhibited a relative phase of 0^o, within experimental error. This implies that these transitions occur very rapidly in time, including the one appearing in the region of $^2E(t^3)$.

$MgO:Cr^{3+}$

Figure 21 shows the room temperature absorption spectrum of $MgO:Cr^{3+}$. Three bands appear, at 3400 Å, 4500 Å, and 6200 Å respectively. The bands at 4500 Å and 6200 Å represent the $^4A_2 \rightarrow {}^4T_1$ and

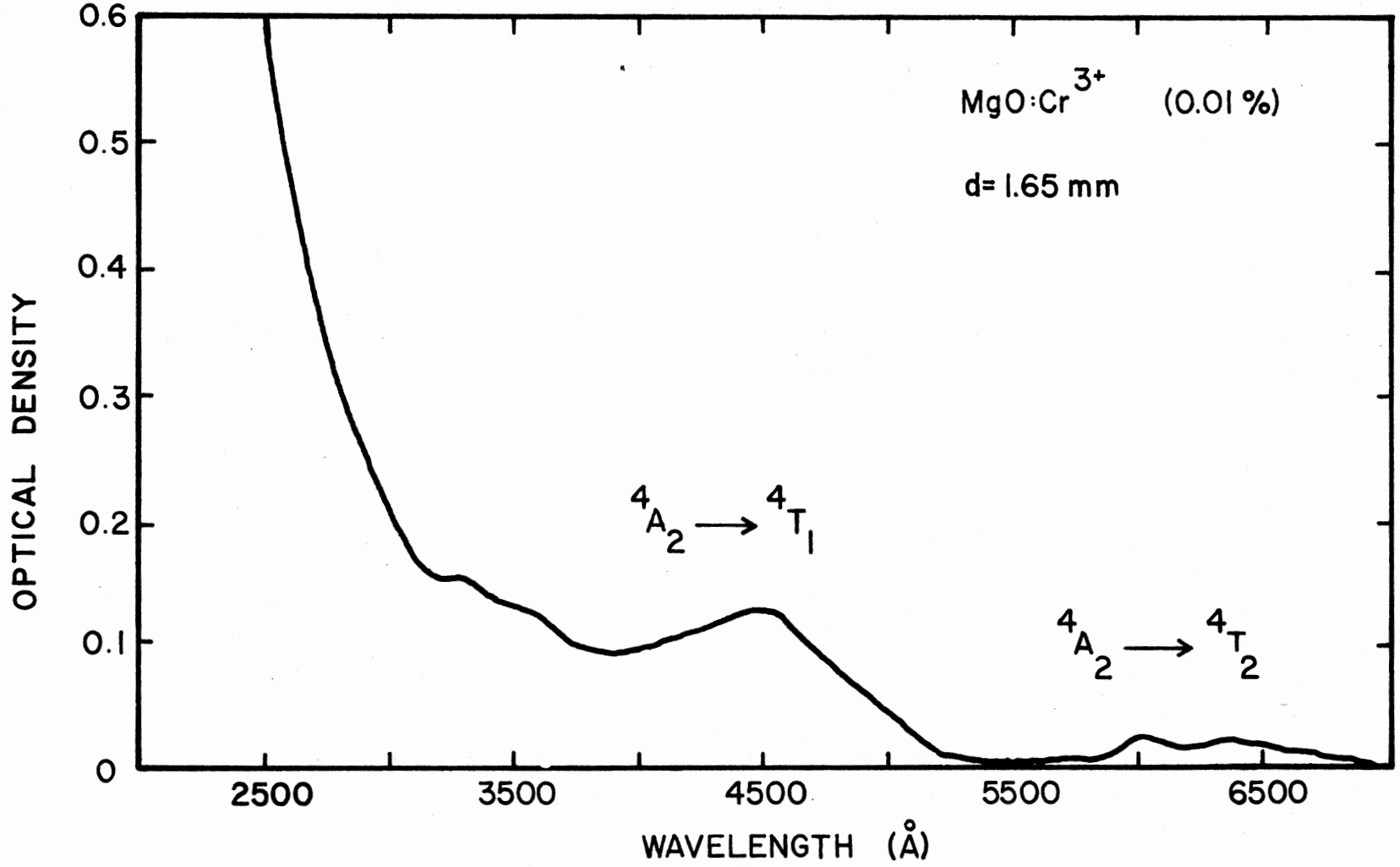

Figure 21. Room Temperature Absorption Spectrum of MgO:Cr^{3+} (0.01%)

$^4A_2 \rightarrow {}^4T_2$ transitions in absorption, with relative peak heights in the ratio 4:1.

TABLE VII

RATIO OF THE INTEGRATED INTENSITIES* OF THE $^4T_1$ AND $^4T_2$ BANDS IN THE ROOM TEMPERATURE ABSORPTION, EXCITATION AND PAS SPECTRA OF $Al_2O_3:Cr^{3+}$ (0.01%)

	$^4T_1$	$^4T_2$	$^4T_1/^4T_2$
Absorption	370	270	1.37
Excitation	520	550	0.95
PAS	230	150	1.53

* Integrated intensities are measured in arbitrary units

Figure 22 shows the $MgO:Cr^{3+}$ excitation spectrum obtained from Henry (25). This particular spectrum is the normalized "cubic" contribution to the composite excitation spectrum, and as such represents the R line excitation spectrum at 77K. Peaks appear at 4330 Å and 6000 Å representing the $^4T_1$ and $^4T_2$ bands respectively. The concentration of the sample used in excitation was 0.05% Cr^{3+}.

Figure 23 shows the normalized room temperature PAS results for $MgO:Cr^{3+}$. Broad bands appear, centered at 4000 Å, 6100 Å, and 6950 Å.

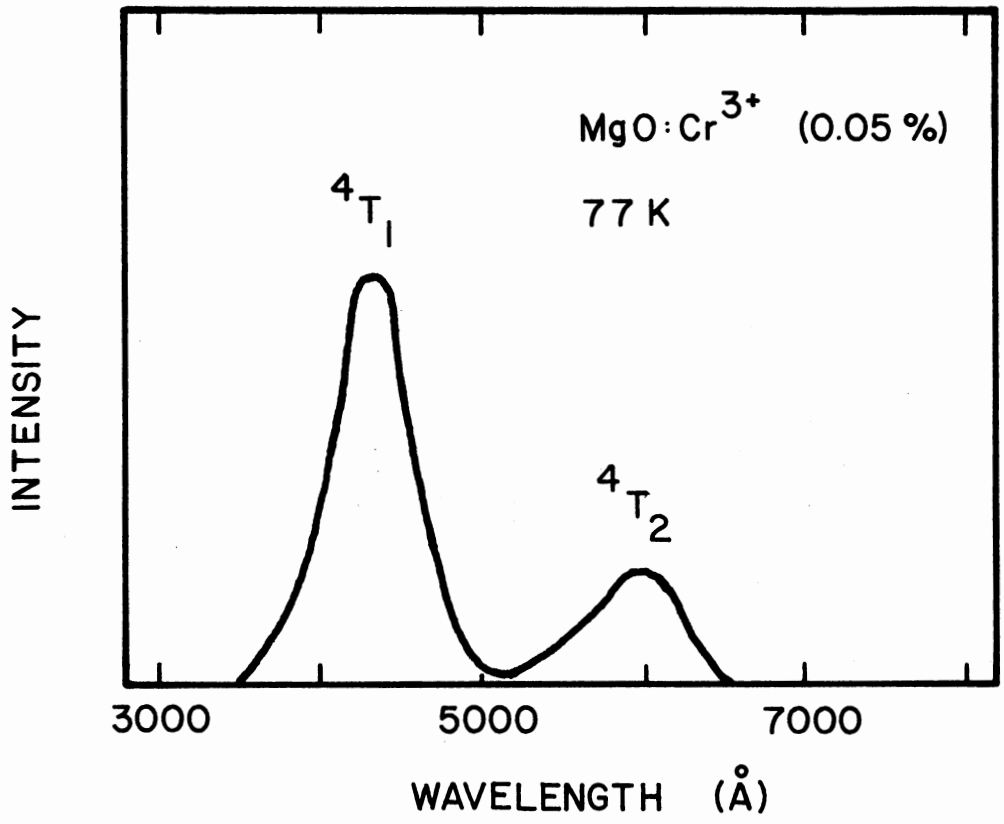

Figure 22. Normalized R Line Excitation Spectrum of MgO:Cr^{3+} at 77K (from Henry, Reference 28; the Spectrum Here Reflects Henry's Correction for the Energy Dependence of the Normalization Curve)

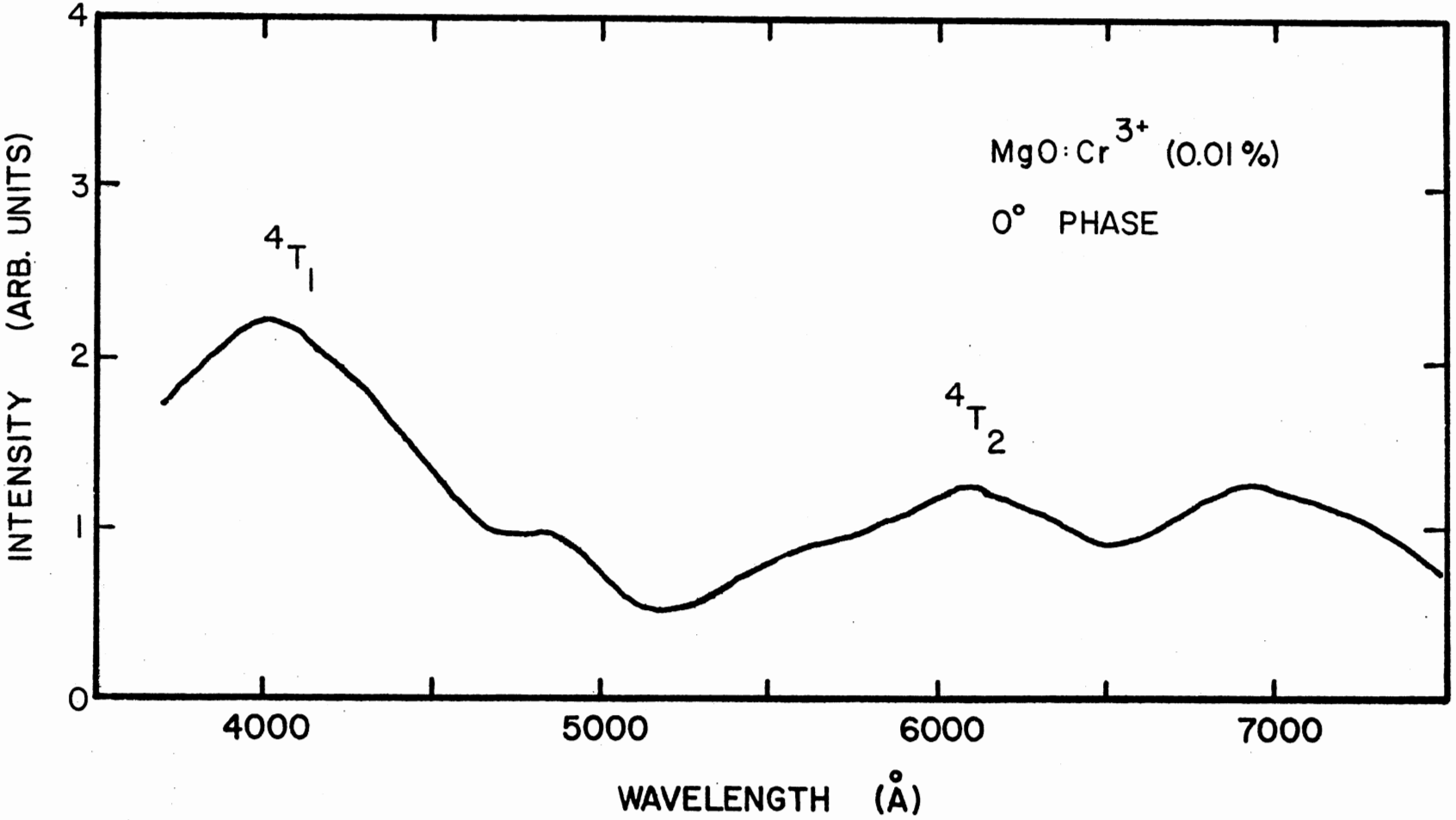

Figure 23. Normalized Room Temperature Photoacoustic Spectrum of MgO:Cr^{3+} (0.01%)

The first two can be associated with the $^4T_1$ and $^4T_2$ chromium bands and the third appears in the general region of the ^2E transition. The $^4T_1$ band appears to be shifted from the position predicted by the absorption and excitation spectra.

The relative intensities of the two major chromium bands and their ratios obtained from the absorption, excitation and PAS spectra are listed in Table VIII. As with ruby all transitions monitored showed 0^o relative phase indicating very fast radiationless decay from these levels.

TABLE VIII

RATIO OF THE INTEGRATED INTENSITIES* OF THE $^4T_1$ AND $^4T_2$ BANDS IN THE ABSORPTION, EXCITATION AND PAS SPECTRA OF MgO:Cr^{3+}

	$^4T_1$	$^4T_2$	$^4T_1/^4T_2$
Absorption	220	30	7.33
Excitation	94**	35	2.68
PAS	360	230	1.56

* Integrated intensities are in arbitrary units

** Reflects lifting of the correction applied by Henry (25) (130 units)(avg. energy of $^4T_2$/avg. energy of $^4T_1$) = 94 units

A brief note should be included here about the nature of $MgO:Cr^{3+}$. Chromium ion in MgO is in a crystal lattice site of octahedral symmetry. However, Henry, Larkin, and Imbusch have shown that there exist significant contributions to the absorption and excitation spectra from tetragonal and rhombic site symmetries (8).

$$SrTiO_3:Cr^{3+}$$

Figure 24 shows the room temperature absorption spectrum of $SrTiO_3:Cr^{3+}$. An absorption edge appears at 3900 Å and a broad band at 5100 Å. Stokowski and Schawlow report that the typical ^4T absorption bands normally seen in Cr^{3+}-doped materials are not seen in the room temperature absorption of $SrTiO_3:Cr^{3+}$ (9). They attribute the strong band at 5100 Å to Ti^{3+} or other defects. The spectrum of Figure 29 corresponds very well with the data published by the above authors. Since the Cr^{3+} absorption bands are completely masked by other absorption only estimates of Cr^{3+} absorption can be made using excitation spectra as a guide.

Figure 25 shows the normalized low temperature excitation spectrum of $SrTiO_3:Cr^{3+}$. These data show a large peak at 3800 Å, corresponding to the excitation of electrons into the conduction band (9), a large shoulder at 4500 Å and a band at 5950 Å. The two latter bands are asigned to the $^4T_1$ and $^4T_2$ chromium transitions respectively. Stokowski and Schawlow present an excitation spectra, taken at 77K showing peaks at 3800 Å, 4700 Å, and 6150 Å, the latter being rather broad. Their data, unfortunately, are not corrected for system response.

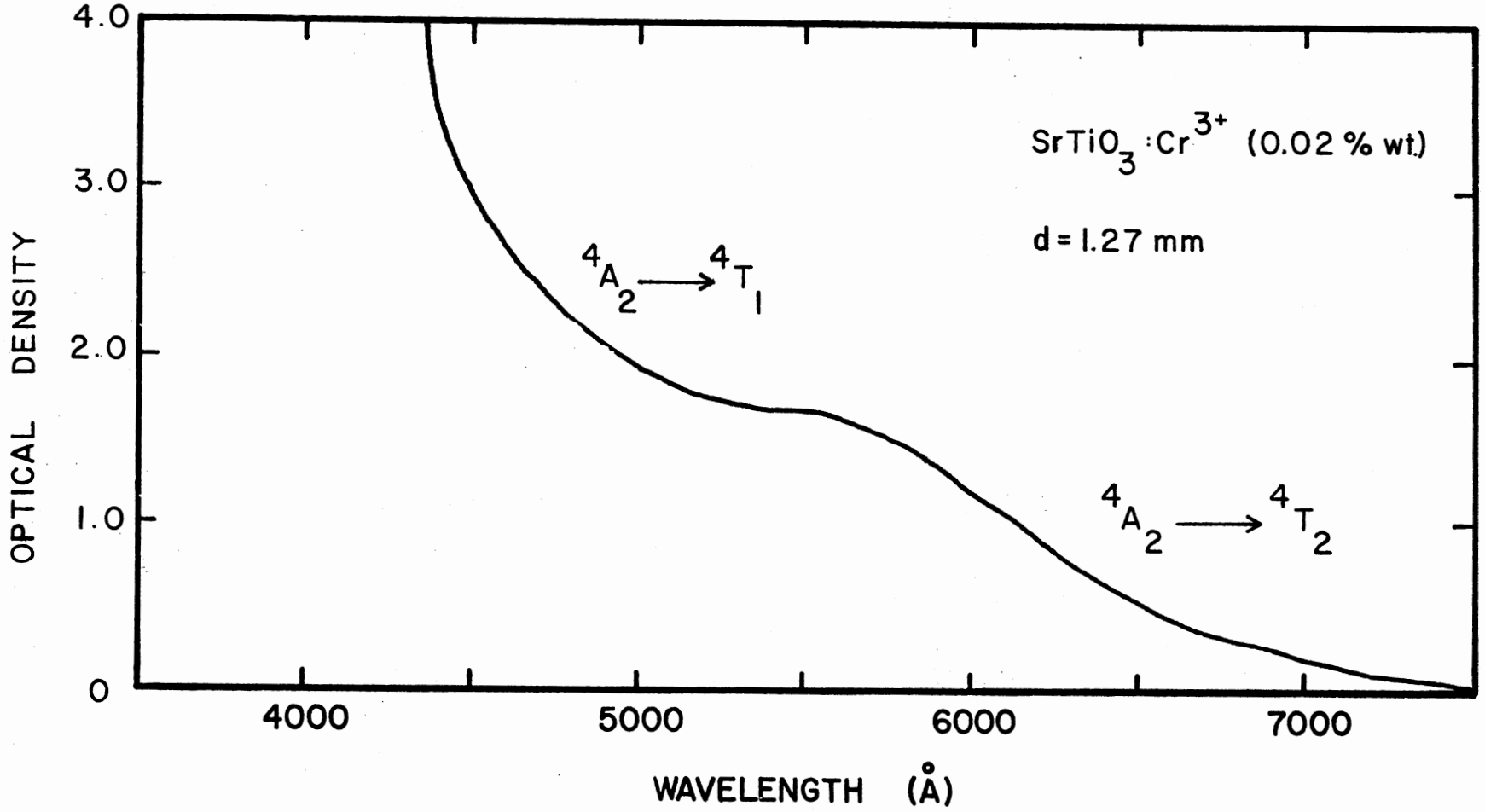

Figure 24. Room Temperatue Absorption Spectrum of $SrTiO_3:Cr^{3+}$

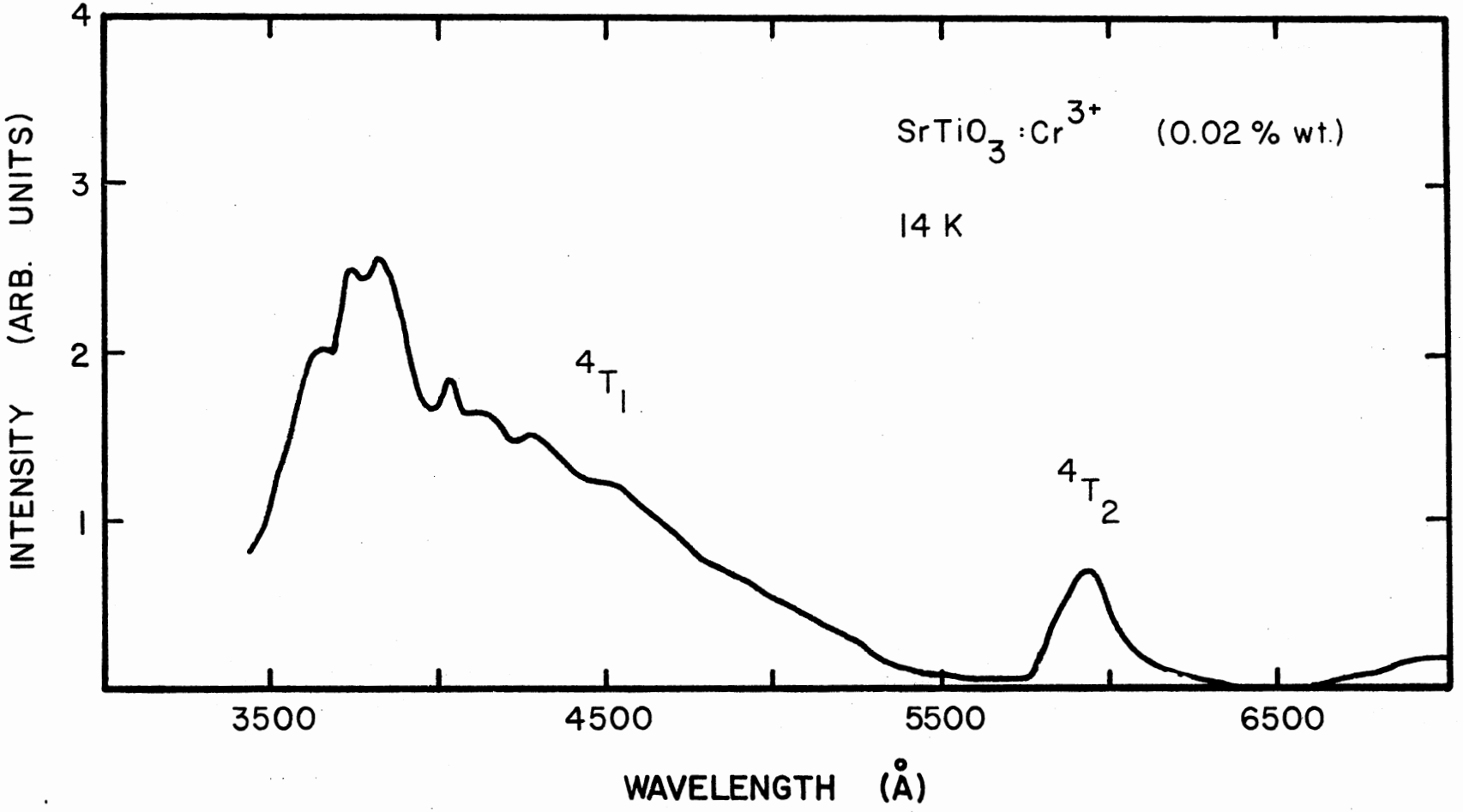

Figure 25. Normalized Low Temperature (14K) Excitation Spectrum of $SrTiO_3:Cr^{3+}$ (0.02% Wt)

Figure 26 shows the normalized room temperature PAS spectrum of $SrTiO_3:Cr^{3+}$. Bands appear at 4350 Å ($^4T_1$) and 6250 Å ($^4T_2$) corresponding to Cr^{3+} transitions, and a band at 5150 Å corresponding most probably to Ti^{3+} or other impurity. The phase of these peaks again proved to be 0^o relative. The relative intensities of these peaks as well as their ratios appear in Table IX. At room temperature Cr^{3+} ion is in a site of cubic symmetry (31) so that no fine structure splitting of Cr^{3+} levels is expected. It is curious that the absorption edge does not appear in the PAS spectrum. A possible explanation is the low power of the lamp below 3900 Å. Previous data taken with the same lamp show no absorption edge, however, an earlier spectrum using a mercury lamp did indicate the absorption edge, beginning about 3900 Å. Work with mercury excitation was suspended later because of a high degree of light scattering into the microphone at higher energies due to the power of the source in this region. Precautions were taken to protect the microphone from such, but they never proved to be satisfactory.

$BaTiO_3:Cr^{3+}$

Figures 27 and 28 indicate the room temperature optical absorption and photoacoustic spectra of $BaTiO_3:Cr^{3+}$. No optical emission was observed in the region 6500-9000 Å for runs carried out at 14K, 120K, and 296K. The PAS spectrum mirrors the behavior of the absorption spectrum with absorption edge at 4300 Å and a broad band centered at 6300 Å. As with $SrTiO_3:Cr^{3+}$ the chromium absorption bands are probably masked by other absorption. The absorption data obtained here compare well with the results of other workers (32,33). As

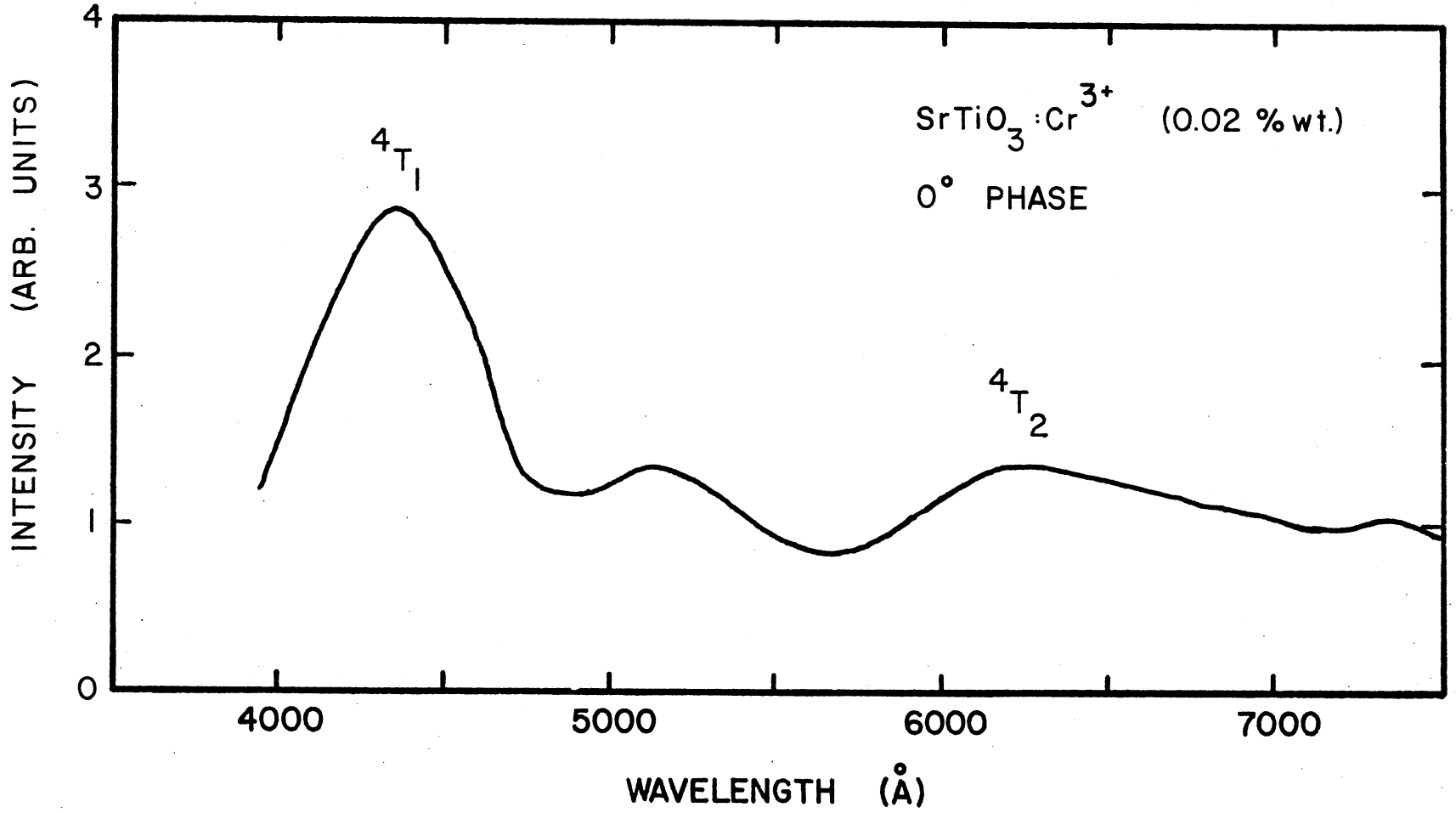

Figure 26. Normalized Room Temperature PAS Spectrum of $SrTiO_3:Cr^{3+}$ (0.02% Wt)

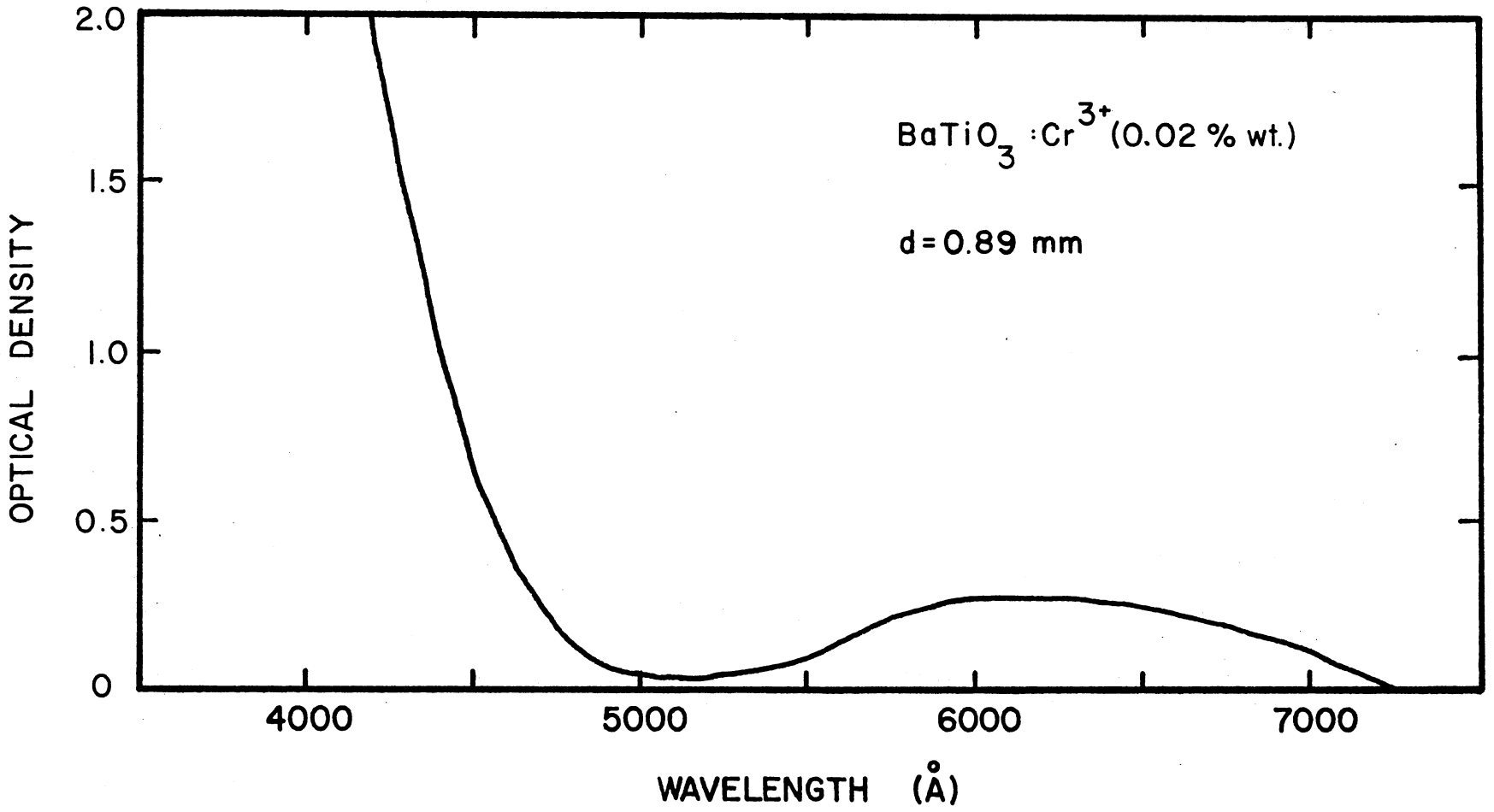

Figure 27. Room Temperature Absorption Spectrum of $BaTiO_3:Cr^{3+}$ (0.02% Wt)

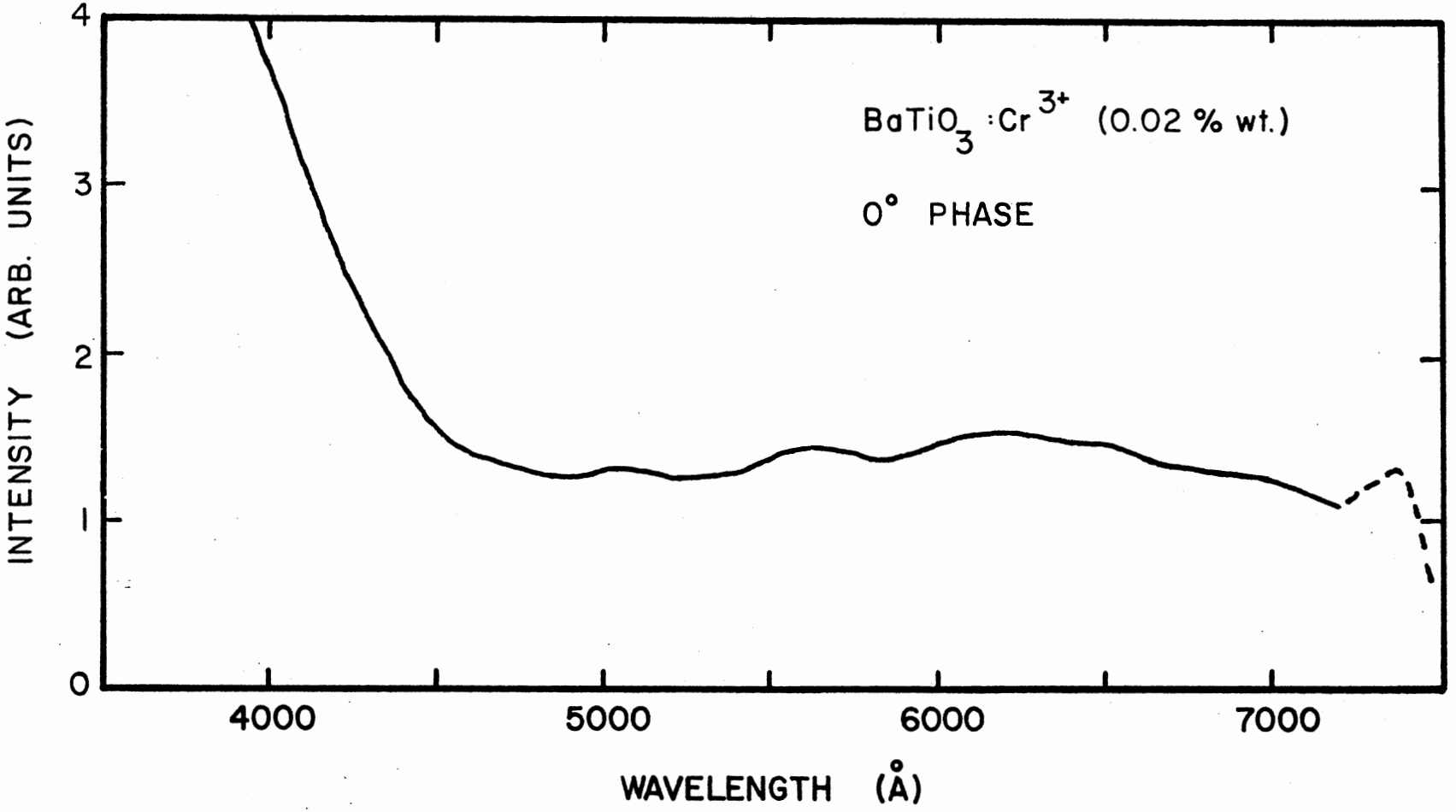

Figure 28. Normalized Room Temperature PAS Spectrum of $BaTiO_3:Cr^{3+}$ (0.02% Wt)

opposed to the PAS spectrum of $SrTiO_3:Cr^{3+}$ the absorption edge is observed in $BaTiO_3:Cr^{3+}$. The latter, however, was a powdered sample giving a much stronger signal. The phase of the PAS signal registered 0^o relative for all regions monitored.

TABLE IX

RATIO OF THE INTEGRATED INTENSITIES* OF THE $^4T_1$ AND $^4T_2$ BANDS IN THE ABSORPTION, EXCITATION AND PAS SPECTRA OF $SrTiO_3:Cr^{3+}$

	$^4T_1$	$^4T_2$	$^4T_1/^4T_2$
Absorption	210	50	4.2
Excitation	150	30	5.0
PAS	370	170	2.18

* Integrated intensities are in arbitrary units

Further Discussion of Experimental Results

As noted above, the $^4T_1$ band in the ruby PAS spectrum is somewhat resolved into its A and E components, with the peak height of the A component about 1.4 times greater than that of E. These same effects appear in the polarized absorption spectra cited previously (28).

This is consistent with the observation that for R line excitation the quantum efficiency of the E band is greater than that of the A band, so that a larger radiationless contribution is expected from $^4T_1$ (A) than from $^4T_1$ (E) (5). The ratio of integrated intensities, $S_{PAS}(^4T_1)/S_{PAS}(^4T_2)$ is approximately 1.5.

The appearance of large photoacoustic signals in the ruby and MgO:Cr^{3+} spectra in the region of the ^2E transition is attributed to some type of absorption process taking place which is not well understood at this time. The PAS bands appear broader and larger than those expected for ^2E absorption and the lifetimes predicted by phase angle analysis are very fast. It is possible that the MgO:Cr^{3+} band observed could come from chromium ions of rhombic site symmetry (7,8,25). However, the presence of a similar band in ruby, where no such sites exist, tends to eliminate such a conclusion.

The spectra of $SrTiO_3$:Cr^{3+} and $BaTiO_3$:Cr^{3+} are less conclusive. The masking of, or probable masking of, the Cr^{3+} absorption bands by other absorption prevents a detailed discussion of these results.

To gain some further insight into the processes taking place a calculation of the observed fraction of absorbed energy converted to heat is performed (5). Consider the following: The ratio of integrated absorption band intensities of $^4T_1$ to $^4T_2$ may be expressed as

$$R_{(ABS)} = \beta(^4T_1)/\beta(^4T_2) \qquad (65)$$

where $\beta(^4T_1)$ and $\beta(^4T_2)$ refer to the integrated intensities of the absorption bands in Figures 18, 21, 24. The ratio of integrated PAS

band signals can be expressed as

$$R_{(PAS)} = S_{PAS}\,(^4T_1) \;/\; S_{PAS}\,(^4T_2) \qquad (66)$$

where S_{PAS} refers to the integrated intensities of the bands in Figures 20, 23, and 26. The ratio of integrated fluorescence excitation bands is written as

$$R_{(EXC)} = S_{EXC}\,(^4T_1) \;/\; S_{EXC}\,(^4T_2) \qquad (67)$$

where S_{EXC} refers to the integrated intensities of the bands in Figures 19, 22, and 25. From Equation (52) a comparable expression to Equation (66) may be obtained, which is written

$$R_{(PAS)} = (\alpha_1/\alpha_2)(\beta_1/\beta_2) \qquad (68)$$

This implies that $(\alpha_1/\alpha_2) = R_{(PAS)}/(\beta_1/\beta_2)$. If substitution of Equation (65) can be made for the term (β_1/β_2) in Equation (68), then the ratio of the fractions of absorbed energy converted to heat can be calculated from the experimental data and is expressed as

$$(\alpha_1/\alpha_2) = R_{(PAS)} \;/\; R_{(ABS)} \qquad (69)$$

The ratio of the fractions of absorbed energy converted to radiative emission can likewise be calculated from the expression

$$(\varepsilon_1/\varepsilon_2) = R_{(EXC)} \;/\; R_{(ABS)} \qquad (70)$$

Table X lists the ratios obtained from Equations (65), (66), (67), (69), and (70) for the $Al_2O_3:Cr^{3+}$, $SrTiO_3:Cr^{3+}$ and $MgO:Cr^{3+}$ data, in that order. Also listed is the observed value of the mean energy of

TABLE X

SELECTED RATIOS* AND PARAMETERS IN THE STUDY OF RADIATIONLESS PROCESSES IN $Al_2O_3:Cr^{3+}$, $SrTiO_3:Cr^{3+}$ AND $MgO:Cr^{3+}$

Sample	$R_{(ABS)}$	$R_{(PAS)}$	$R_{(EXC)}$	(α_1/α_2)	$(\varepsilon_1/\varepsilon_2)$	$\tilde{\nu}_{10Dq}(cm^{-1})$
$Al_2O_3:Cr^{3+}$	1.37	1.53	0.95	1.12	0.69	17,857
$SrTiO_3:Cr^{3+}$	4.2	2.18	5.0	0.52	1.19	16,667
$MgO:Cr^{3+}$	7.33	1.56	2.68	0.21	0.36	16,129

* See text for explanation of symbols and parameters.

the $^4T_2$ band in each of the three materials. The values for $(\varepsilon_1/\varepsilon_2)$ show no detectable trend for the order of samples listed. However, (α_1/α_2) does show a trend, which is decreasing in nature. This decreasing trend is matched by a similar decreasing trend in the value of $\tilde{\nu}_{10Dq}$, the average energy of the $^4T_2$ band. The decreasing value of $\tilde{\nu}_{10Dq}$ is an indication of lessening influence from crystal field splitting and of a decrease in the static coupling to the lattice. The decrease in the value of the ratio (α_1/α_2) is similar to results obtained by Murphy and Aamodt for increasing concentrations of Cr^{3+} in ruby samples (5).

Avenues of Radiationless Decay

Figure 29 indicates the energy level diagram of chromium ion in ruby (34). The nonradiative decay rates for transitions between the various levels, as calculated by Fonger and Struck (6) are also shown in the figure. Using this diagram as a model two general paths of radiationless decay are apparent. The first is direct decay from the excited state energy levels to the ground state. According to Fonger and Struck (6) this route of deexcitation has a rate of approximately 10^{-27} to 10^4 per second at zero Kelvin. The second route encompasses a cascading of deexcitation through the energy levels until ^2E is reached, which subsequently deexcites radiatively. The inter-level nonradiative rates for this decay route are much greater, ranging from 10^4 to 10^{13} per second. The larger decay rates indicate much shorter lifetimes for transitions incorporating this mode of decay. The relative size of the phase angle measured photoacoustically is also a measure of the lifetime of the nonradiative decay. Smaller angles

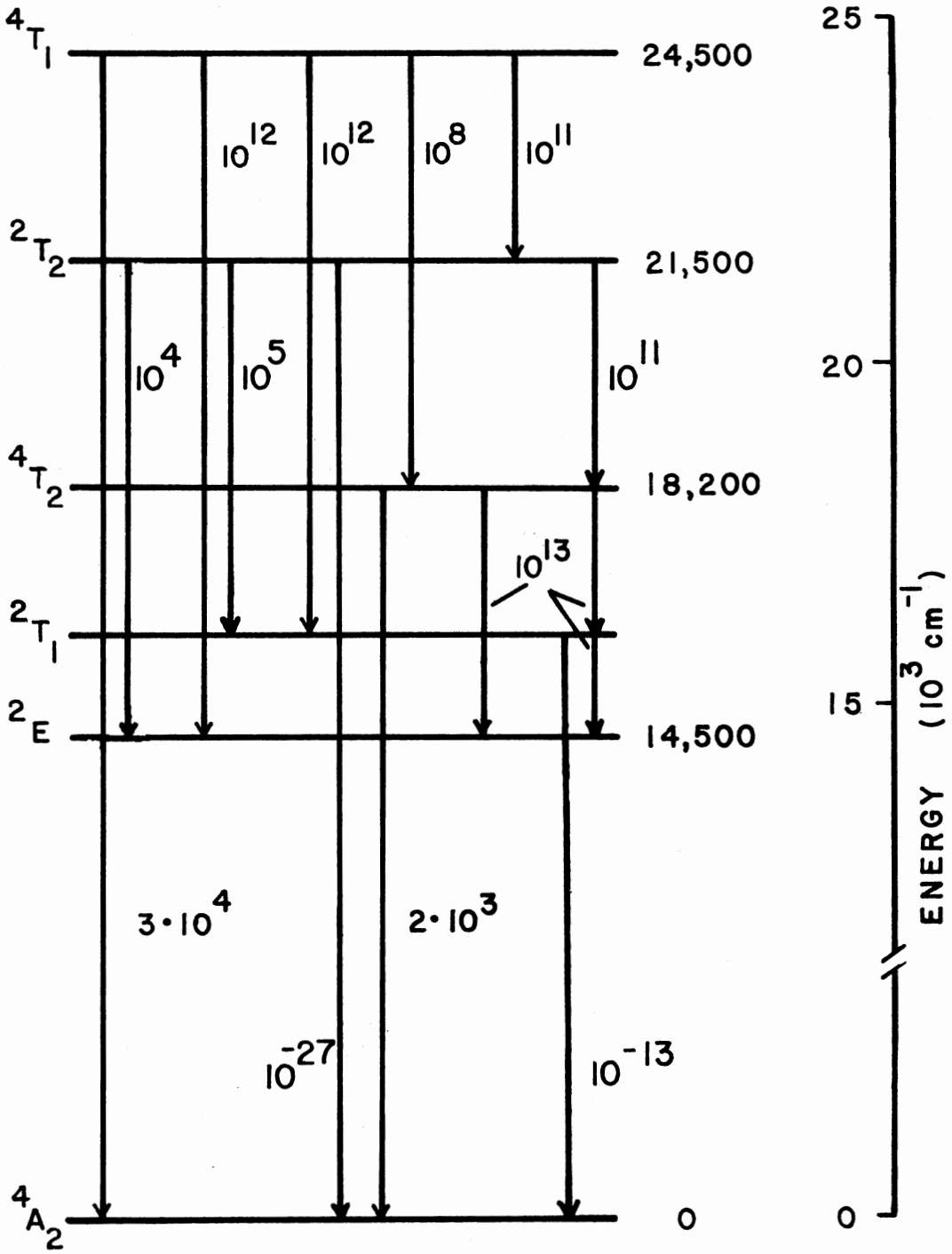

Figure 29. Energy Level Diagram of the Chromium Bands in Ruby Indicating Nonradiative Transition Rates

indicate shorter lifetimes. The phase angles determined experimentally for ruby (and in fact all four samples) consistently registered zero degrees. Even within the instrumental error of $\pm 3^{o}$ this result indicates a very fast decay from all positions monitored. Thus it would seem that the second mode of decay, the inter-level cascade, is preferred in ruby over the direct, band to ground state transition. This conclusion is substantiated by results reported by Robin and Kuebler (7) obtained from thermometric measurements. With excitation into the broad bands lying above ^{2}E, their results show a very fast heat pulse at short times followed by a slow rise and fall of temperature, longer in time and characteristic of relaxation from the ^{2}E level.

Further evidence that ruby prefers the cascading decay channel is provided by the following:

Consider a crystal having an energy level E which deexcites radiatively. The excitation signal strength of this level when pumped from a higher lying absorption band (labeled one) can be expressed as

$$\varepsilon_1' = \beta_1 \, \phi_{nr} \, (1-E) \, h\nu_E \, / \, h\nu_1 \qquad (71)$$

where β_1 denotes the absorption strength of this level, $\phi_{nr}(1-E)$ represents the nonradiative "quantum efficiency" of a transition between band level one and level E, $h\nu_E$ is the energy of the radiative emission and $h\nu_1$ is the correction factor for the spectral distribution of the lamp-monochromator combination. This depends upon the energy of band level one. The ratio of excitation signal strengths of two bands, labeled one and two, can then be expressed as

$$\frac{\varepsilon_1'}{\varepsilon_2'} = \frac{\beta_1}{\beta_2} \, \frac{\phi_{nr}(1-E)h\nu_2}{\phi_{nr}(2-E)h\nu_1} \qquad (72)$$

Dividing out the relative absorption strengths of the two levels (performed by dividing Equation (72) by Equation (65)) leaves an expression which is equal to the ratio of the fractions of absorbed light converted to radiative emission through level E

$$\frac{\varepsilon_1}{\varepsilon_2} = \frac{\phi_{nr}\ (1-E)h\nu_2}{\phi_{nr}\ (2-E)h\nu_1} \tag{73}$$

Equation (73) is completely comparable to Equation (70).

The PAS signal strength of a radiationless decay between level one and level E for a fast signal at 0^o phase is expressed as

$$\alpha_1' = \beta_1\phi_{nr}(1-E)h\nu(1-E)/h\nu_1 \tag{74}$$

where the same designations prevail here as in Equation (71). The factor $h\nu(1-E)$ represents the fact that the PAS signal strength depends on the energy of the phonon liberated. More energetic phonons give rise to more heat and thus a stronger signal. The ratio of the PAS signal strengths for bands one and two is expressed as

$$\frac{\alpha_1'}{\alpha_2'} = \frac{\beta_1}{\beta_2}\ \frac{\phi_{nr}(1-E)h\nu(1-E)h\nu_2}{\phi_{nr}(2-E)h\nu(2-E)h\nu_1} \tag{75}$$

By again dividing out the relative absorption strengths of the two bands an expression for the ratio of the fractions of absorbed light converted to heat results;

$$\frac{\alpha_1}{\alpha_2} = \frac{\phi_{nr}(1-E)h\nu(1-E)h\nu_2}{\phi_{nr}(2-E)h\nu(2-E)h\nu_1} \tag{76}$$

For two levels which decay radiationlessly through a cascade to a radiating level E, the ratio of the fractions of absorbed light converted to radiative emission and the ratio of the fractions of absorbed light converted to heat ought to be equivalent. Thus the expression for $(\varepsilon_1/\varepsilon_2)$ in Equation (73) ought to be equal to the expression for (α_1/α_2) in Equation (76), except for the factor $h\nu(1-E)/h\nu(2-E)$ in Equation (76). But this factor enters in only because of the nature of the energy conversion process in PAS. Thus, in any system where the proposed avenue of radiationless decay is a fast cascade down to an emitting level, the following expression should hold:

$$\frac{\varepsilon_1}{\varepsilon_2} = \frac{\alpha_1}{\alpha_2} \frac{h\nu(2-E)}{h\nu(1-E)} \qquad (77)$$

This is exactly what is postulated in the ruby example. Table XI lists the terms found on the left and right hand sides of Equation (77) for each of the three samples, following the same order as in Table X. In Table XI level one refers to the chromium $^4T_1$ band, level two to the $^4T_2$ band and level E to the ^2E level. Thus $h\nu(2-E)$ is the energy difference between levels $^4T_2$ and E, peak to peak, and $h\nu(1-E)$, the difference between $^4T_1$ and E. The values for (α_1/α_2) and $(\varepsilon_1/\varepsilon_2)$ are taken from Table X.

Within the accuracy of this study the values for ruby in the third and fourth columns of Table XI are equivalent, substantiating the conclusion drawn earlier that the avenue of radiationless decay in this material is an inter-level cascade down to level ^2E instead of a direct transition from the excited state levels to the ground state. Due to the inequivalence of the values of these same parameters in

$MgO:Cr^{3+}$ and $SrTiO_3:Cr^{3+}$ it is concluded that other paths of radiationless decay must also be present in these materials.

TABLE XI

MEASUREMENT OF THE DEGREE OF RADIATIONLESS CONVERSION THROUGH THE CASCADE CHANNEL

Sample	(α_1/α_2)	$\frac{h\nu(2-E)}{h\nu(1-E)}$*	$\frac{\alpha_1 h\nu(2-E)}{\alpha_2 h\nu(1-E)}$	$(\varepsilon_1/\varepsilon_2)$
$Al_2O_3:Cr^{3+}$	1.12	0.47	0.53	0.69
$SrTiO_3:Cr^{3+}$	0.52	0.33	0.17	1.19
$MgO:Cr^{3+}$	0.21	0.20	0.04	0.36

* Energy values derived from Figures 20, 23, and 26.

Figure 30 shows the energy level diagram of $MgO:Cr^{3+}$ for chromium ions occupying sites of cubic symmetry (34). The two general routes of nonradiative decay from excited levels are indicated. The inter-level cascade down to ^2E as the sole means of radiationless deexcitation has been eliminated through the use of the values listed in Table XI. The mode of decay might be a mixture of deexcitations through both channels. In a crystal where not only radiationless transitions from level one to E and level two to E are allowed but also transitions

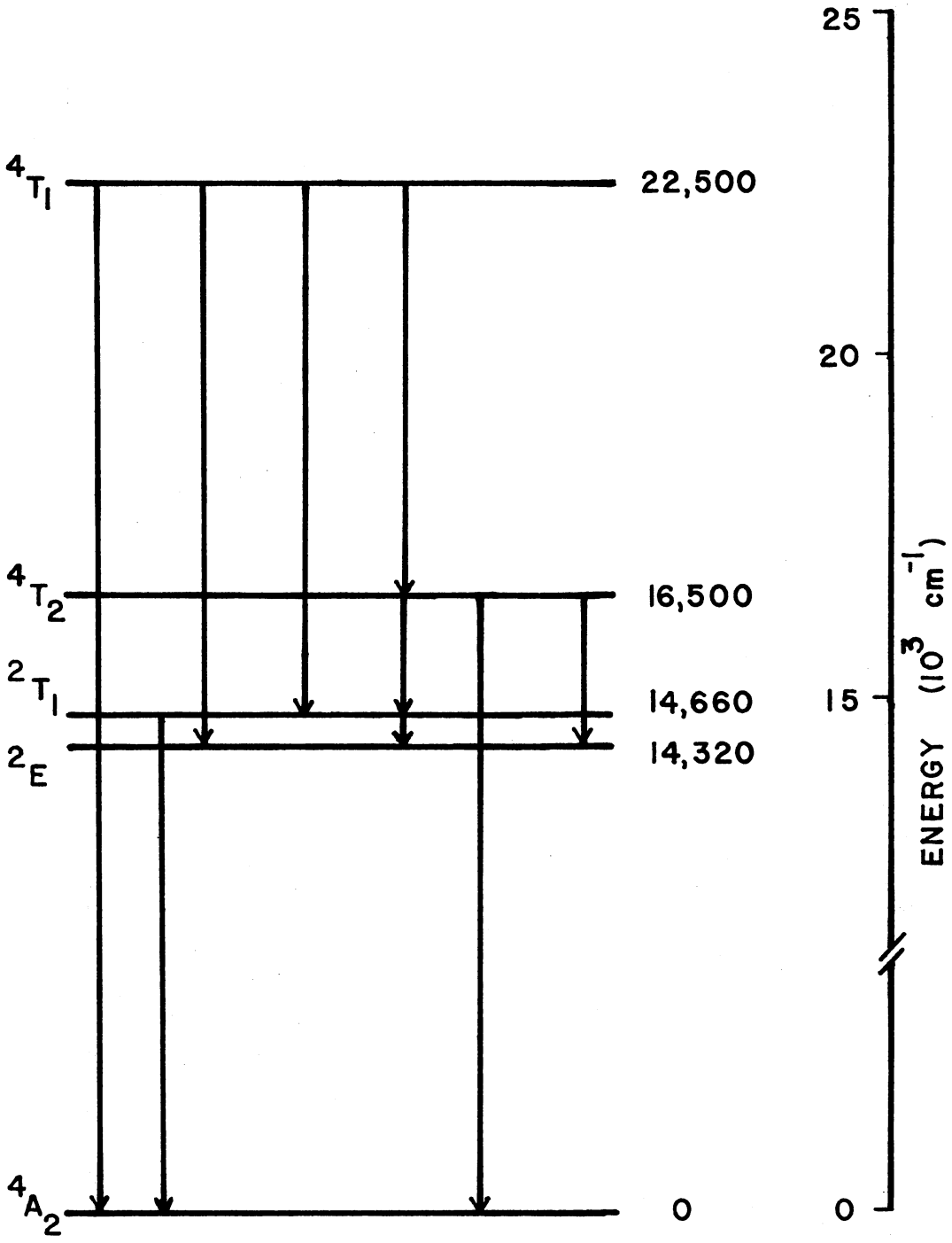

Figure 30. Energy Level Scheme for MgO:Cr^{3+} (Cubic Symmetry) Showing Possible Paths of Radiationless Deexcitation

from level one to the ground state (A) and level two to the ground state Equation (76) is re-expressed as

$$\frac{\alpha_1}{\alpha_2} = \frac{h\nu_2}{h\nu_1} \frac{[\phi_{nr}(1\text{-}E)h\nu(1\text{-}E) + \phi_{nr}(1\text{-}A)h\nu(1\text{-}A)]}{[\phi_{nr}(2\text{-}E)h\nu(2\text{-}E) + \phi_{nr}(2\text{-}A)h\nu(2\text{-}A)]} \tag{78}$$

In order to simplify the evaluation of Equation (78), assume that no radiationless decay from level one to A occurs. This implies that the term $\phi_{nr}(1\text{-}A)$ vanishes, and Equation (78) becomes

$$\frac{\alpha_1}{\alpha_2} = \frac{h\nu_2}{h\nu_1} \frac{\phi_{nr}(1\text{-}E)h\nu(1\text{-}E)}{\phi_{nr}(2\text{-}E)h\nu(2\text{-}E)} \cdot \left[\frac{1}{1 + \frac{\phi_{nr}(2\text{-}A)h\nu(2\text{-}A)}{\phi_{nr}(2\text{-}E)h\nu(2\text{-}E)}}\right] \tag{79}$$

Multiplying both sides of Equation (79) by the factor $h\nu(2\text{-}E)/h\nu(1\text{-}E)$ yields

$$\frac{\alpha_1}{\alpha_2} \frac{h\nu(2\text{-}E)}{h\nu(1\text{-}E)} = \frac{h\nu_2}{h\nu_1} \frac{\phi_{nr}(1\text{-}E)}{\phi_{nr}(2\text{-}E)} \cdot \left[\frac{1}{1 + \frac{\phi_{nr}(2\text{-}A)h\nu(2\text{-}A)}{\phi_{nr}(2\text{-}E)h\nu(2\text{-}E)}}\right]$$

$$= \frac{\varepsilon_1}{\varepsilon_2} \cdot \left[\frac{1}{1 + \frac{\phi_{nr}(2\text{-}A)h\nu(2\text{-}A)}{\phi_{nr}(2\text{-}E)h\nu(2\text{-}E)}}\right] \tag{80}$$

Values for the left side and the first term on the right side of Equation (80) can be obtained from Table XI. Values for the energy terms can also be calculated. Substituting these values into Equation (80) predicts that the ratio $\phi_{nr}(2\text{-}A)/\phi_{nr}(2\text{-}E)$ have a value near unity.

This implies equal contributions from both avenues of decay from level $^4T_2$ which does not seem reasonable for the following reason: It was seen in ruby that the prime decay route was an inter-level cascade. This means that $\phi_{nr}(2\text{-}A)$ is very small in ruby and that $\phi_{nr}(2\text{-}E)$ has a value of almost unity. Due to the approximate equivalence of the $^4T_2$ band Huang-Rhys factors in ruby and MgO:Cr^{3+} (2000 cm^{-1} versus 2176 cm^{-1}), the value of $\phi_{nr}(2\text{-}E)$ in MgO:Cr^{3+} is also presumed to be near unity. Thus the value of the ratio $\phi_{nr}(2\text{-}A)/\phi_{nr}(2\text{-}E)$ in MgO:Cr^{3+} cannot be unity. Additional modes of radiationless decay must be present, other than those evaluated above, or some perturbing factor is present in MgO:Cr^{3+} which greatly affects the calculations used to determine paths of nonradiative relaxation. It was mentioned earlier that there are significant contributions from chromium ions of tetragonal and rhombic site symmetries. Henry, Larkin, and Imbusch (8) have drawn attention to the fact that the rhombic $^4T_2$ level lies lower than the cubic ^2E level. Thus the only reasonable mode of decay from this level is directly to the ground state. All three types of Cr^{3+} sites were probed in the experiments without differentiation so that it may be postulated that the perturbing influence of these different sites is a potential cause of the difficulties in describing the proper avenue of decay in MgO:Cr^{3+}.

Similar computations could be performed for $SrTiO_3$:Cr^{3+} provided sufficient data were available. The masking of the Cr^{3+} bands in absorption makes any prediction of processes in $SrTiO_3$:Cr^{3+} extremely tenuous.

CHAPTER VI

SUMMARY

Laser excitation into the long wavelength tail of the host absorption band of rare-earth doped calcium tungstate crystals directly excites activator-induced tungstate defects sites which transfer energy to their nearest neighbor activator ions in a single step process. The type of transfer mechanism involved could be either electric dipole-dipole or exchange interaction since each is capable of predicting sufficient energy transfer to account for the rates determined experimentally. These results uphold the idea (3) that the type of host-sensitized energy transfer process occurring is dependent upon the wavelength of excitation used. The existence of activator-induced tungstate defect sites surrounding the activator ions is supported by the evidence of the directly excitable sites observed in this investigation.

It would be interesting and perhaps useful in future applications to see if similar wavelength dependent excitations would produce related or dissimilar results in other systems. Common phosphors such as the molybdates and vanadates might prove to be interesting target materials. The tentative plans to use a frequency up-converter to laser excite into the higher energy absorption bands in order to investigate narrow band excitation into these regions and to compare

these results with those obtained for broad band excitation could prove to be very interesting.

The results of the Photoacoustic Spectroscopy study indicate that the preferred mode of radiationless decay in ruby is a cascade from higher lying levels down to the ^2E level, which emits radiatively, instead of by direct transitions to the ground state. PAS phase angle analysis predicts very fast lifetimes for the transitions observed, which helps to substantiate this conclusion. These fast rates of decay are similar to results reported by other workers (7).

The preferred mode of radiationless deexcitation in $MgO:Cr^{3+}$ remains unclear. It seems evident that a simple cascade such as occurs in ruby does not take place. Significant contributions from chromium ions occupying sites of rhombic symmetry may add to the problem.

The spectra of $SrTiO_3:Cr^{3+}$ and probably $BaTiO_3:Cr^{3+}$ are masked by other absorption, adding difficulty to a clear interpretation of the results (9).

Calculations using the PAS results indicate a trend towards increasing $^4T_2$ level contributions to radiationless decay as the static coupling to the lattice and the effects of crystal field splitting decrease.

Photoacoustic Spectroscopy can be a fairly powerful technique in elucidating characteristics of radiationless decay. It is suggested that a continuous wave, scanning dye laser system be employed to improve on the signal strength and resolution of future experiments. An investigation into the absorption characteristics in the ^2E region of ruby

and $MgO:Cr^{3+}$ is needed to identify the source of the fast lifetime PAS signals observed in the spectra at these wavelengths. With the improvements that the laser system would provide an improved study of the experiments conducted for this dissertation could be performed.

BIBLIOGRAPHY

1. Kröger, F. A., Some Aspects of the Luminescence of Solids (Elsevier Publishing Co., New York, 1948).

2. Botden, Th. P. J., Philips Res. Rep. 6, 425 (1951).

3. Treadaway, M. J. and R. C. Powell, Phys. Rev. B11, 862 (1975).

4. Treadaway, M. J. and R. C. Powell, J. Chem. Phys. 61, 4003 (1974).

5. Murphy, J. C. and L. C. Aamodt, to be published.

6. Fonger, W. H. and C. W. Struck, Phys. Rev. B11, 3251 (1975).

7. Robin, M. B. and N. A. Kuebler, to be published.

8. Henry, M. O., J. P. Larkin, and G. F. Imbusch, Phys. Rev. B13, 1893 (1976).

9. Stokowski, S. E. and A. L. Schawlow, Phys. Rev. 178, 457 (1969).

10. Dexter, O. L., J. Chem. Phys. 21, 836 (1953).

11. Treadaway, M. J., Ph.D. Dissertation, Oklahoma State University (1974), unpublished.

12. Förster, T., Z. Naturforsch. A4, 321 (1949).

13. Förster, T., Ann. Physik 2, 55 (1948).

14. Inokuti, M. and F. Hirayama, J. Chem. Phys. 43, 1978 (1965).

15. Parker, J. G., App. Opt. 12, 2974 (1973).

16. Rosencwaig, A., Opt. Comm. 7, 305 (1973).

17. Rosencwaig, A., Science 181, 657 (1975).

18. Rosencwaig, A., Physics Today 28, 23 (1975).

19. Rosencwaig, A., Anal. Chem. 47, 593 (1975).

20. Merkle, L. D. and R. C. Powell, Chem. Phys. Lett. 46, 303 (1977).

21. Aamodt, L. C., J. C. Murphy and J. G. Parker, J. Appl. Phys. 48, 303 (1977).

22. Rosencwaig, A. and A. Gersho, J. Appl. Phys. 47, 64 (1976).

23. Kim, Q., R. C. Powell, M. Mostroller, and T. M. Wilson, Phys. Rev. B12, 5627 (1975).

24. Boyrivent, A., E. Duval and R. Louat, Solid State Comm. 19, 1221 (1976).

25. Henry, M. O., Ph.D. Thesis, University College, Galway, Ireland (1976), unpulished.

26. Brecker, C., et al., Phys. Rev. 155, 178 (1967).

27. Reed, E. D., Jr. and H. W. Moos, Phys. Rev. B8, 988 (1973).

28. McClure, D. S., J. Chem. Phys. 36, 2757 (1962).

29. Powell, R. C., AFCRL 66-830, "The Interaction of Chromium Ions in Ruby Crystals," December, 1966.

30. Misu, A., J. Phys. Soc. Japan 19, 2260 (1964), as reported in Reference (29).

31. Müller, K. A., in Paramagnetic Resonance, edited by W. Low (Academic Press, Inc., New York 1963, Vol. 1) as reported in Reference (9).

32. Ikegami, S., I. Ueda and Y. Ise, J. Phys. Soc. Japan 16, 572 (1961).

33. Bursian, E. V., Ya. G. Girshberg, and E. N. Starov, Phys. Stat. Solidi (B) 46, 529 (1971).

34. Imbusch, G. F., private communication.

VITA

Robert Glen Peterson

Candidate for the Degree of

Doctor of Philosophy

Thesis: ENERGY TRANSFER AND DISSIPATION PROCESSES IN DOPED CRYSTALS

Major Field: Physics

Biographical:

Personal Data: Born in Bartlesville, Oklahoma, March 23, 1947, the son of Glen and Doreyn L. Peterson.

Education: Graduated from Nathan Hale High School, Tulsa, Oklahoma, in May, 1965; received Bachelor of Science degree in Physics from Brigham Young University in 1971; received Master of Science degree in Biophysics from Brigham Young University in 1974; completed requirements for the Doctor of Philosophy degree at Oklahoma State University in December, 1977.

Professional Experience: Graduate Teaching Assistant, Department of Physics, Brigham Young University, 1971-73; Assistant Chief Engineer, Magnalectric Corporation, 1973-74; Graduate Teaching and Research Assistant, Department of Physics, Oklahoma State University, 1975-77.

Professional Organizations: Member, Institute of Electrical and Electronics Engineers.